



MOJAVE. XIX. Brightness Temperatures and Intrinsic Properties of Blazar Jets

D. C. Homan¹, M. H. Cohen², T. Hovatta^{3,4}, K. I. Kellermann⁵, Y. Y. Kovalev^{6,7,8}, M. L. Lister⁹, A. V. Popkov^{6,7},
A. B. Pushkarev^{6,7,10}, E. Ros⁸, and T. Savolainen^{4,8,11}

¹ Department of Physics and Astronomy, Denison University, Granville, OH 43023, USA; homand@denison.edu

² Department of Astronomy, California Institute of Technology, Pasadena, CA 91125, USA

³ Finnish Centre for Astronomy with ESO, FINCA, University of Turku, Finland

⁴ Aalto University Metsähovi Radio Observatory, Metsähovintie 114, FI-02540 Kylmälä, Finland

⁵ National Radio Astronomy Observatory, 520 Edgemont Road, Charlottesville, VA 22903, USA

⁶ Lebedev Physical Institute of the Russian Academy of Sciences, Leninsky prospekt 53, 119991 Moscow, Russia

⁷ Moscow Institute of Physics and Technology, Institutsky per. 9, Dolgoprudny, Moscow region, 141700, Russia

⁸ Max-Planck-Institut für Radioastronomie, Auf dem Hügel 69, D-53121 Bonn, Germany

⁹ Department of Physics and Astronomy, Purdue University, 525 Northwestern Avenue, West Lafayette, IN 47907, USA

¹⁰ Crimean Astrophysical Observatory, 298409 Nauchny, Crimea¹², Russia

¹¹ Aalto University Department of Electronics and Nanoengineering, PL 15500, FI-00076 Aalto, Finland

Received 2021 August 9; revised 2021 September 8; accepted 2021 September 9; published 2021 December 10

Abstract

We present multiepoch, parsec-scale core brightness temperature observations of 447 active galactic nucleus (AGN) jets from the MOJAVE and 2 cm Survey programs at 15 GHz from 1994 to 2019. The brightness temperature of each jet over time is characterized by its median value and variability. We find that the range of median brightness temperatures for AGN jets in our sample is much larger than the variations within individual jets, consistent with Doppler boosting being the primary difference between the brightness temperatures of jets in their median state. We combine the observed median brightness temperatures with apparent jet speed measurements to find the typical intrinsic Gaussian brightness temperature of $4.1(\pm 0.6) \times 10^{10}$ K, suggesting that jet cores are at or below equipartition between particle and magnetic field energy in their median state. We use this value to derive estimates for the Doppler factor for every source in our sample. For the 309 jets with both apparent speed and brightness temperature data, we estimate their Lorentz factors and viewing angles to the line of sight. Within the BL Lac optical class, we find that high-synchrotron-peaked BL Lacs have smaller Doppler factors, lower Lorentz factors, and larger angles to the line of sight than intermediate and low-synchrotron-peaked BL Lacs. We confirm that AGN jets with larger Doppler factors measured in their parsec-scale radio cores are more likely to be detected in γ rays, and we find a strong correlation between γ -ray luminosity and Doppler factor for the detected sources.

Unified Astronomy Thesaurus concepts: Active galaxies (17); Galaxy jets (601); Radio galaxies (1343); Quasars (1319); BL Lacertae objects (158); Surveys (1671)

Supporting material: figure set, machine-readable tables

1. Introduction

Extragalactic jets from active galactic nuclei (AGN) flow outward from the central supermassive black hole (SMBH)/accretion disk system at nearly the speed of light, and for observers at a small angle to the jet direction, emission from the approaching jet is Doppler boosted and variable, creating some of the most spectacular displays in the universe. The relativistic charged particles and magnetic fields that comprise the jets create broadband synchrotron and inverse Compton emission that together span the observable spectrum from radio to TeV γ -rays, and the jets may serve as a source of high-energy neutrino emission as well (e.g., IceCube Collaboration et al. 2018; Aartsen et al. 2020; Kovalev et al. 2020a; Plavin et al. 2020, 2021; Hovatta et al. 2021).

Unfortunately, the extreme nature of these jets also complicates our study of their intrinsic properties and physical processes. In addition to Doppler boosting of the intrinsic emission, the flow of the jets toward us at nearly the speed of light leads to a compression of the apparent timescale, creating observed “superluminal” motions (e.g., Cohen et al. 1971) in the jets with

$\beta_{\text{obs}} = \beta \sin \theta / (1 - \beta \cos \theta)$, where β is the intrinsic speed and θ is the angle the jet axis makes with the line of sight. To untangle these effects, we need to measure both the observed speed of the jet and its Doppler factor, $\delta = 1/[\Gamma(1 - \beta \cos \theta)]$, where $\Gamma = 1/\sqrt{1 - \beta^2}$ is the Lorentz factor of the flow; however, Doppler factors are extraordinarily difficult to measure in synchrotron jets, as they lack sharp spectral features of a known wavelength.

Readhead (1994) suggested using the apparent brightness temperatures of jet cores measured at radio wavelengths, along with an assumption of equipartition between magnetic field and particle energy in the emission region to estimate jet Doppler factors. The radio jet core in Very Long Baseline Interferometry (VLBI) images is the apparent base of the jet where the transition from optically thin to optically thick emission occurs. In the frame of the host galaxy, the Doppler boosted observed brightness temperature in the direction of the observer is given by $T_{\text{b,obs}} = \delta T_{\text{b,int}}$, where $T_{\text{b,int}}$ is the intrinsic, un-boosted brightness temperature of the region.¹³ The assumption of equipartition between field and particle energy has been used

¹² While the AAS journals adhere to and respect UN resolutions regarding the designations of territories (available at <http://www.un.org/press/en>), it is our policy to use the affiliations provided by our authors on published articles.

¹³ Note that variability brightness temperatures include two additional powers of δ due to the estimation of the angular size by the variability timescale (e.g., Lähteenmäki & Valtaoja 1999).

by a number of authors to estimate Doppler factors from either VLBI data (e.g., Guijosa & Daly 1996; Tingay et al. 2001) or integrated flux density variability (e.g., Lähteenmäki & Valtaoja 1999; Hovatta et al. 2009; Liodakis et al. 2017).

Homan et al. (2006) showed that it was possible to estimate a global value for $T_{b,int}$ directly from VLBI apparent motion and brightness temperature data without the need to assume equipartition or any other ratio of particle to magnetic field energy, and recently Liodakis et al. (2018) used Doppler factor distributions from population models to constrain $T_{b,int}$ independent of the assumption of equipartition. We also note that the VLBI-based flux-density variability approach of Jorstad et al. (2005) can estimate the Doppler factor of a moving jet feature from its angular size and variability timescale without any assumptions about its brightness temperature.

In this paper we present multiepoch, parsec-scale core brightness temperature observations of 447 AGN jets from the MOJAVE program (e.g., Lister & Homan 2005; Lister et al. 2018), and we combine those observations with apparent speed measurements in 309 of our jets by Lister et al. (2021, hereafter *MOJAVEXVIII*). We use our multiepoch Very Long Baseline Array (VLBA) observations from the entire available span of the MOJAVE and 2 cm Survey programs, from 1994 to 2019, to characterize the brightness temperature of each jet core over time by its median value and variability, and by comparing the jets to one another in their median state, we strengthen our confidence that a single representative value of $T_{b,int}$ can apply broadly across our sample. Rather than assume equipartition, we follow Homan et al. (2006) and combine our median brightness temperature observations with apparent speed measurements to estimate the global value for $T_{b,int}$. As a result of this analysis, we obtain estimates of the Doppler factor for almost every source in our sample, and for the 309 jets where we have apparent speed measurements, we also estimate their Lorentz factors and jet viewing angles to the line of sight. We compare these intrinsic properties between sources as a function of their optical class, spectral energy distribution (SED) peak frequency, and γ -ray properties, and we discuss the implications of our measurement of $T_{b,int}$ for the energy balance between particles and magnetic fields in jet cores.

The paper is organized as follows. In Section 2, we describe our data analysis, including both our methods for measuring brightness temperatures and for combining those measurements with apparent jet speeds to find $T_{b,int}$ and estimate the intrinsic properties of the jets. In Section 3, we present and discuss our results, and we summarize our conclusions in Section 4. We assume a Λ CDM cosmology with $H_0 = 71 \text{ km s}^{-1} \text{ Mpc}^{-1}$, $\Omega_\Lambda = 0.73$, and $\Omega_M = 0.27$ (Komatsu et al. 2009) throughout the paper.

2. Data Analysis

Our sample consists of the 447 AGN recently studied by the MOJAVE program for kinematics in *MOJAVEXVIII*, of which 206 are members of the MOJAVE 1.5 Jy quarter-century (QC) flux-density-limited sample selected on the basis of parsec-scale jet emission (e.g., Lister et al. 2019). Our whole sample of 447 AGN includes sources that are outside the 1.5 Jy QC sample added over the years for a variety of reasons, including their high energy emission and membership in other AGN-monitoring programs, but all have a minimum 15 GHz correlated flux density larger than $\sim 50 \text{ mJy}$ and J2000 declinations $> -30^\circ$ as described in *MOJAVEXVIII*. Table 1 lists the sources in our sample along with several of their properties. For each source we measure its core brightness temperature as described in Section 2.1 in all the 15

GHz VLBA epochs analyzed by our program through 2019 August 6, and in Section 2.2 we describe our method that combines the brightness temperature observations with apparent speeds from *MOJAVEXVIII* to estimate Doppler factors (δ) Lorentz factors (Γ) and viewing angles to the line of sight (θ) for sources that have the necessary information.

2.1. Measuring Core Brightness Temperatures

We measure the brightness temperature in the core region in each epoch by fitting a single elliptical Gaussian in the (u, v) -plane. The core region is isolated by first starting with our final CLEAN image of the jet and using the Caltech VLBI program, DIFMAP (Shepherd 1997, 2011), to delete the CLEAN components around the core location in an area equal in size to the full-width half-maximum dimensions of the naturally weighted beam. In some cases, this area may be enlarged somewhat if doing so reduces the final χ^2 of the fitted Gaussian. The central location for the area from which the CLEAN components are deleted is either the pixel closest to the core location as used in our kinematics fits (*MOJAVEXVIII*) or the nearest local maximum if a local maximum can be found within half a beamwidth of the kinematics core location. The deleted CLEAN components are replaced with a single elliptical Gaussian, which is fitted in the (u, v) -plane. The result is a hybrid Gaussian/CLEAN component model, with the Gaussian properties representing the core region (near optical depth equals unity) and with CLEAN components modeling the remainder of the source structure.

Figure 1 illustrates this technique by showing the inner jet of the source 0003+380 over its first six epochs. Because the entire core region is modeled by a single Gaussian, this approach will average over any substructure, and will occasionally lead to noisier than average fits, such as in the second epoch illustrated in Figure 1. In this epoch, a newly emerging feature in the jet is not sufficiently distinct from the core region to be modeled by the CLEAN components directly. In these cases, it is tempting to fit a second Gaussian component, and indeed we experimented with a multi-Gaussian approach. However, it is difficult to define robust criteria under which two Gaussians should replace a single Gaussian while still producing a reliable brightness temperature measurement of the core region. By sticking to a single Gaussian in all cases, we ensure consistency across epochs and between sources while allowing that there will be times where the emergence of a new feature may enlarge the core region and possibly reduce the measured brightness temperature. We report measured brightness temperatures in the frame of the host galaxy as the peak brightness temperature of the fitted Gaussian (e.g., Kovalev et al. 2005)

$$T_b = 1.22 \times 10^{12} \frac{S_G(1+z)}{\Omega_{\text{maj}}\Omega_{\text{min}}\nu_{\text{obs}}^2} \text{ K}, \quad (1)$$

where z is the source redshift, S_G is the integrated flux density of the fitted Gaussian in Jy, $\Omega_{\text{maj},\text{min}}$ are the full-width half-maximum (FWHM) dimensions of the Gaussian in milliarcseconds, and ν_{obs} is the observing frequency in GHz. The result is in the rest frame of the host galaxy. Table 2 lists the properties of the brightness temperature fit in every epoch for each source. Upper limits on our measured angular sizes were determined in one of two ways: either (1) following Kovalev et al. (2005) where the signal to noise ratio $S/N = S_G/\sigma_{\text{rms}}$, or (2) by enlarging the angular size of the fitted Gaussian until the normalized χ^2 of the fit increased by 1.0. Unresolved features

Table 1
Source Properties

Source	Alias	z	Class	MOJ 1.5	Spectrum	$\nu_{\text{peak,obs}}$ (\log_{10} Hz)	L_{γ} (\log_{10} erg s $^{-1}$)	References
(1)	(2)	(3)	(4)	(5)	(6)	(7)	(8)	(9)
0003+380	S4 0003+38	0.229	Q	N	LSP	13.14	45.12	Schramm et al. (1994), 1
0003-066	NRAO 005	0.3467	B	Y	LSP	12.92	44.81	Jones et al. (2005), 2
0006+061	TXS 0006+061	...	B	N	LSP	13.44	...	Rau et al. (2012), 1
0007+106	III Zw 2	0.0893	G	Y	LSP	13.30	...	Sargent (1970), 3
0010+405	4C +40.01	0.256	Q	N	LSP	12.79	44.59	Thompson et al. (1992), 2
0011+189	RGB J0013+191	0.477	B	N	LSP	13.67	45.41	Shaw et al. (2013b), 2
0012+610	4C +60.01	...	U	N	LSP	13.11,1
0014+813	S5 0014+813	3.382	Q	N	LSP	12.50	...	Varshalovich et al. (1987), 3
0015-054	PMN J0017-0512	0.226	Q	N	LSP	13.60	45.27	Shaw et al. (2012), 1
0016+731	S5 0016+73	1.781	Q	Y	LSP	12.32	47.91	Lawrence et al. (1986), 2
...								

Note. The complete version of this table appears in the online journal. Columns are as follows: (1) source name in B1950.0 coordinates; (2) alias; (3) redshift; (4) optical class (Q = quasar, B = BL Lac, G = radio galaxy, N = narrow-line Seyfert 1, U = unknown); (5) member of the MOJAVE 1.5 Jy QC sample (Y = yes, N = no); (6) SED class (LSP/ISP/HSP = low/intermediate/high-synchrotron-peaked); (7) SED peak in observer frame; (8) γ -ray luminosity, computed as described in Section 3.1.1; and (9) references for redshift/optical classification. SED property references are as follows: 1 = Ackermann et al. (2015), 2 = The Fermi-LAT Collaboration (2020), 3 = ASDFit, Stratta et al. (2011), 4 = Meyer et al. (2011), 5 = Xiong et al. (2015), 6 = Chang et al. (2017), 7 = Nieppola et al. (2008), 8 = Ajello et al. (2017), 9 = Ackermann et al. (2011), 10 = Abdo et al. (2009a), 11 = Nieppola et al. (2006), 12 = Chang et al. (2019), 13 = Abdo et al. (2009b), and 14 = Hervet et al. (2015).

(This table is available in its entirety in machine-readable form.)

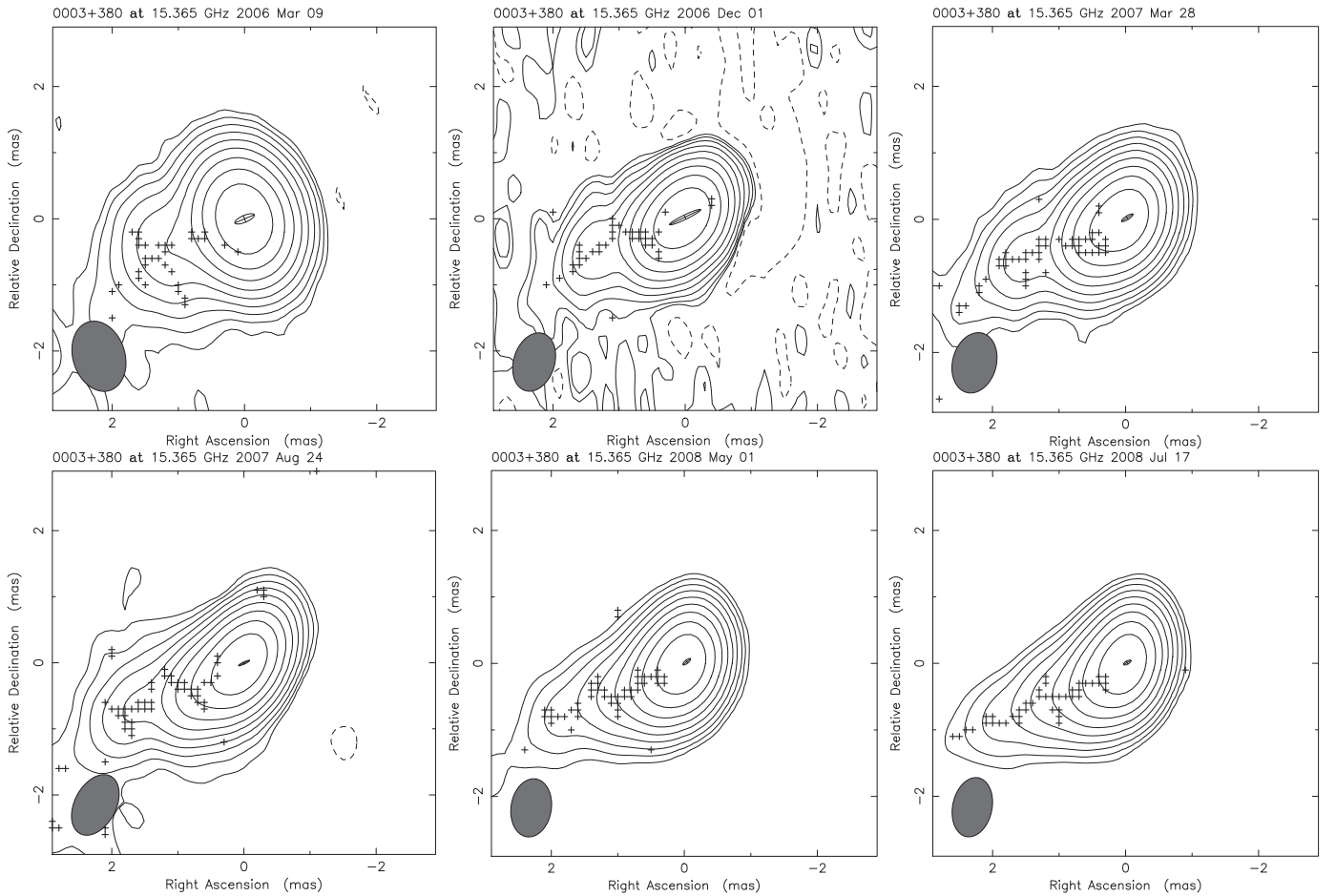


Figure 1. Naturally weighted images illustrating the modeling of the core region of 0003+380 in our first six epochs. Contours begin at 0.2% and increase in factors of two until 51.2% of the peak intensity of 0.543, 0.363, 0.427, 0.417, 0.601, 0.545 Jy beam $^{-1}$ in each epoch respectively. The full-width half-maximum (FWHM) dimensions of the restoring beam are illustrated by the filled ellipse in the lower left corner of each image. As described in the text, CLEAN components (crosses) from the core region are replaced by a single Gaussian component (ellipse). The increased noise in the second epoch is due to a newly emerging feature that is too close to the core to be resolved by this procedure, as described in Section 2.

Table 2
Brightness Temperature Fitting Results

Source (1)	Epoch (2)	ν_{obs} (GHz) (3)	B_{maj} (mas) (4)	B_{min} (mas) (5)	B_{PA} (deg) (6)	C_x (mas) (7)	C_y (mas) (8)	C_{fact} (9)	S_G (Jy) (10)	Ω_{maj} (mas) (11)	Ω_{min} (mas) (12)	Ω_{PA} (deg) (13)	σ_{rms} (mJy bm^{-1}) (14)	T_b (\log_{10} K) (15)
0003+380	2006 Mar 9	15.37	1.01	0.73	17.6	0.0	0.0	1.00	0.586	0.317	0.103	-67.1	1.90	11.057
	2006 Dec 1	15.37	0.85	0.58	-17.4	0.0	0.0	1.00	0.433	0.520	0.067	-64.3	4.00	10.893
	2007 Mar 28	15.37	0.86	0.61	-14.9	0.0	0.0	1.00	0.399	0.200	0.056	-57.8	1.45	11.356
	2007 Aug 24	15.37	0.92	0.58	-28.1	0.0	0.0	1.00	0.408	0.185	<0.036	-65.1	1.17	>11.594
	2008 May 1	15.37	0.82	0.57	-9.1	0.0	0.0	1.00	0.545	0.146	0.049	-51.2	0.159	11.682
	2008 Jul 17	15.37	0.84	0.55	-11.9	0.0	0.0	1.00	0.511	0.126	0.049	-61.1	0.203	11.721
	2009 Mar 25	15.36	0.85	0.62	-12.3	0.0	0.0	1.00	0.346	0.284	<0.060	-63.6	2.31	>11.107
	2010 Jul 12	15.36	0.89	0.54	-12.3	0.0	0.0	1.00	0.378	0.325	0.067	-71.4	2.50	11.041
	2011 Jun 6	15.36	0.91	0.54	-10.2	0.0	0.0	1.00	0.472	0.138	0.061	-61.0	0.371	11.553
2013 Aug 12	15.36	0.84	0.53	-4.1	0.0	0.0	1.00	0.581	0.159	0.045	-61.6	0.846	11.713	
0118-272	2009 Dec 26	15.36	1.43	0.50	-6.7	-0.1	0.1	1.00	0.195	0.186	0.097	-33.9	0.156	>10.746 ^a
	2010 Sep 17	15.36	1.52	0.49	-6.9	0.0	0.0	1.00	0.190	0.181	0.076	-27.9	0.154	>10.856 ^a
	2011 Jul 15	15.36	1.46	0.52	-7.7	0.0	0.0	1.00	0.179	0.155	0.056	-35.9	0.216	>11.029 ^a
	2012 Jul 12	15.36	1.61	0.48	-10.4	0.0	0.0	1.00	0.192	0.243	0.083	-23.9	0.325	>10.693 ^a
	2013 Jul 8	15.36	1.42	0.50	-3.3	0.0	0.0	1.00	0.263	0.183	0.048	-21.4	0.543	>11.188 ^a

Note. The complete version of this table appears in the online journal. Columns are as follows: (1) source name in B1950.0 coordinates; (2) epoch; (3) central observing frequency; (4)–(6) dimensions of naturally weighed beam; (7)–(8) center location of removed clean component area; (9) factor times beam dimensions used for removing clean components; (10) flux density of fitted Gaussian; (11)–(13) dimensions of fitted Gaussian and its position angle; (14) rms residual noise in a region twice the beam dimensions centered at (C_x, C_y) ; and (15) peak brightness temperature of the fitted Gaussian in rest frame of host galaxy.

^a Lower limit value ($z = 0$) only on account of unknown source redshift.

(This table is available in its entirety in machine-readable form.)

have their upper limit size reported as the larger of methods (1) and (2) in Table 2.

To test the validity of our approach, we generated a set of optically thin, homogeneous spherical models, each with 1.0 Jy of flux density but a range of diameters: 0.010, 0.025, 0.050, 0.100, 0.250, 0.500, 1.000, and 2.000 mas. This range of size encompasses completely unresolved structure all the way through objects with significant structure beyond the one-beam area around the center where the Gaussian will be fitted. We used the National Radio Astronomy Observatory’s AIPS package (Greisen 2003) UVMOD task to substitute these models and thermal noise into the (u, v) -coverage of several epochs of two different sources: 0415+379 and 1510-089. The goal here was to see how this approach to measuring brightness temperature might depend on (u, v) -coverage as it varies over epochs or between sources. Each resulting simulated data set was first CLEAN’ed in the same fashion as our MOJAVE data and then analyzed using the approach described above. With the exception of a small fraction of cases, almost all of the models with diameters <0.050 mas were unresolved, while most of those with diameters 0.050 mas or larger were resolved. For each source/diameter combination of 0.050 mas or larger, we were able to extract a median Gaussian peak brightness temperature across the simulated epochs and compare to the expected brightness temperature at the center of the sphere for the corresponding case. We should not expect a ratio of 1.0, as a Gaussian is more sharply peaked than a sphere, and indeed, we found the average ratio was 1.81. This ratio was roughly the same from 0.050 through 2.000 mas with a standard deviation of 0.15 and no trend with assumed sphere diameter, indicating that in the large diameter cases the remaining CLEAN components that represent the extended parts of the structure do not affect the ability of the Gaussian to represent the brightness temperature at the center. Note that in

five of our six resolved models, the source template with low decl. (u, v) -coverage had a larger median brightness temperature resulting in an average difference of $10\% \pm 4\%$ compared to the high decl. template, so differing (u, v) -coverage between sources may introduce a modest level of uncertainty into our measurements.

As an important aside, the ratio of 1.8 between the expected central brightness temperature of a homogeneous sphere and the measured Gaussian peak brightness temperature illustrates the point that brightness temperatures derived from fitted Gaussian parameters may be too large in regions that are not peaked as sharply as a Gaussian. It is difficult to know how the brightness distribution of the inhomogeneous base of a possibly conical or parabolic jet will be represented by the single Gaussian fits used in this analysis, so some caution should be used in interpreting these temperatures directly in terms of the energy balance between magnetic fields and particles in the jet, discussed in Section 3.3; however, we note that this constant geometrical factor does not affect any other aspect of our analysis as it simply divides out of our estimates of the Doppler factor.¹⁴

Figure 2 shows plots of our brightness temperature measurements over time for each source. The median value, 25% value and 75% value of the measured distribution for each source are indicated by black, blue, and red lines, respectively, and are tabulated in Table 3. Because some of our brightness temperature measurements are lower limits, we determine both the lower bound and (where possible) the upper bound on these characteristic points in the distribution. If both lower and upper bounds are available, the characteristic point is taken to be their

¹⁴ This is because $\delta = T_{\text{b,obs}}/T_{\text{b,int}}$ and both quantities include the same geometrical factor given our method for determining $T_{\text{b,int}}$ described in Section 2.2.2.

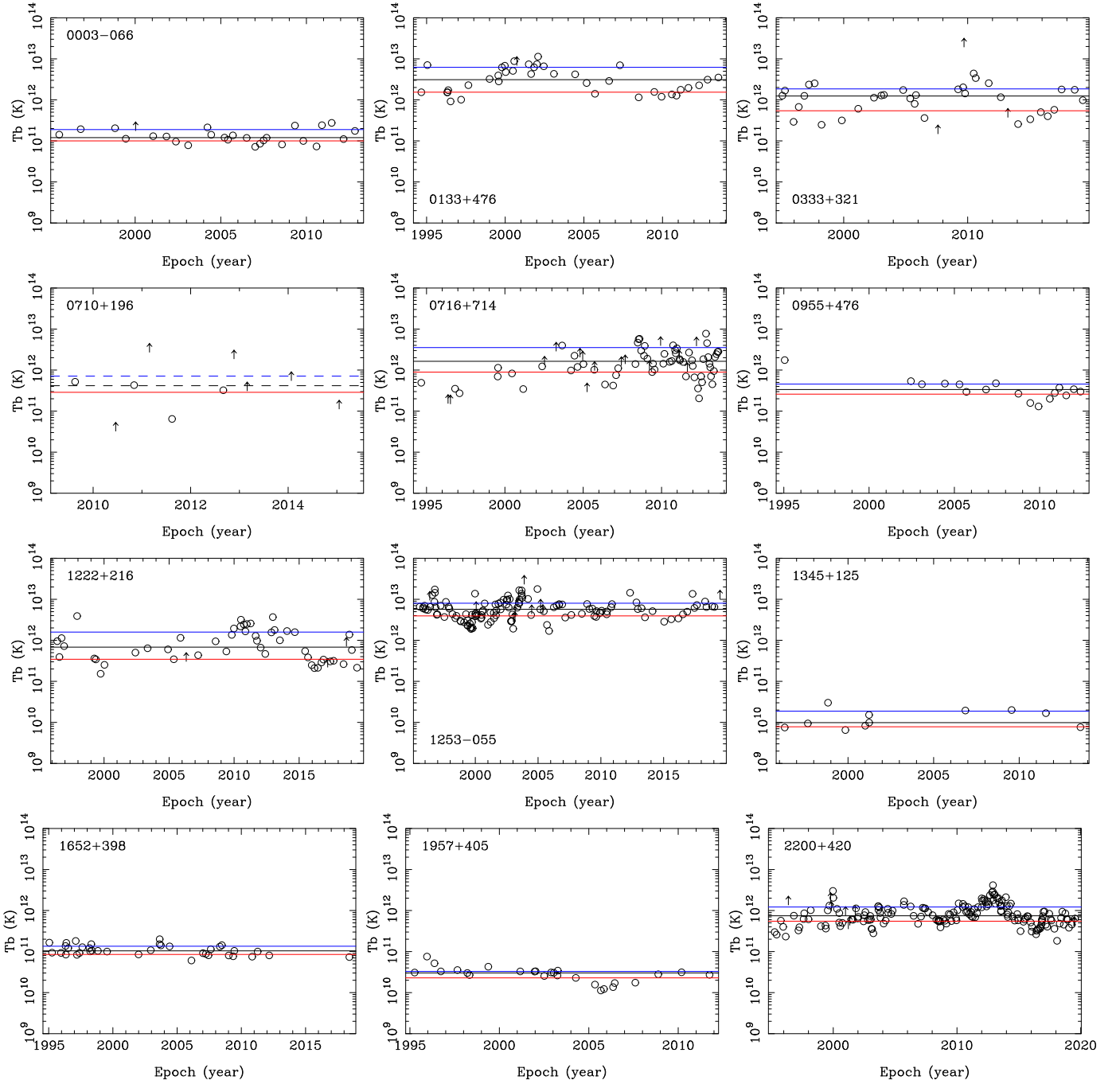


Figure 2. Plots of brightness temperature vs. epoch for each source. The full set of plots for all 447 sources in our sample appears online. Open circles and upward arrows represent measurements and lower limits, respectively. Estimates of the median value of the distribution are shown as black lines; blue and red lines indicate estimates of the 75% and 25% points, respectively. Dashed lines are used when only a lower limit can be placed on these values. Sources with unknown redshifts are plotted with open triangles and dotted lines to represent values that otherwise would be considered measurements but are too small by an unknown factor of $(1+z)$. (The complete figure set (447 images) is available.)

average. Lower bounds on the median and other characteristic points are determined by treating all limits as measurements. We then establish an upper bound on these points by moving all limits to the upper end of the distribution. In some cases, too many individual points are limits, and determining an upper bound on the 25%, median, or 75% point is not possible. In these cases the lower bound is listed as a lower limit in Table 3 and indicated by a dashed line in Figure 2. Distributions of the

median Gaussian peak brightness temperature for each source are presented in Figure 3 and discussed in Section 3.1.1.

We use the 25% and 75% points in the distribution to also define a T_b variability index for each source, which is analogous to that defined by Aller et al. (1992),

$$V_{75,25} = \frac{T_{b,75} - T_{b,25}}{T_{b,75} + T_{b,25}}, \quad (2)$$

Table 3
Brightness Temperatures and Apparent Speeds

Source	N	$T_{b,\min}$ (\log_{10} K)	$T_{b,25}$ (\log_{10} K)	$T_{b,\text{med}}$ (\log_{10} K)	$T_{b,75}$ (\log_{10} K)	$T_{b,\max}$ (\log_{10} K)	$V_{75,25}$	N_s	β_{\max}	β_{med}	β_{close}
(1)	(2)	(3)	(4)	(5)	(6)	(7)	(8)	(9)	(10)	(11)	(12)
0003+380	10	10.893	11.057	11.550	11.702	11.721	0.631	3	4.61 ± 0.36	2.30 ± 0.63	0.57 ± 0.15
0003-066	27	10.857	11.000	11.079	11.276	11.439	0.305	9	7.08 ± 0.21	2.48 ± 0.49	1.868 ± 0.093
0006+061	5	$>10.662^a$	$>10.917^a$	>11.021	>11.049	$>11.064^a$	>0.152
0007+106	25	10.766	11.243	11.729	12.004	12.260	0.705	2	1.58 ± 0.29	1.47 ± 0.18	1.58 ± 0.29
0010+405	12	>11.201	>11.330	>11.425	>11.534	>11.633	...	1	6.92 ± 0.64	6.92 ± 0.64	6.92 ± 0.64
0011+189	8	>10.859	>10.992	>11.207	>11.250	>11.593	...	1	4.54 ± 0.46	4.54 ± 0.46	4.54 ± 0.46
0012+610	6	$>10.684^a$	$>10.684^a$	$>10.747^a$	$>10.843^a$	$>11.086^a$	0.181
0014+813	14	11.029	11.079	11.223	11.354	11.438	0.306	2	9.47 ± 0.91	9.4 ± 1.2	9.3 ± 1.5
0015-054	8	10.436	10.908	11.246	>11.410	>11.629	>0.521
0016+731	16	10.676	11.584	11.902	12.384	12.801	0.726	2	7.64 ± 0.32	5.10 ± 0.22	2.57 ± 0.12
						...					

Notes. The complete version of this table appears in the online journal. Columns are as follows: (1) source name in B1950.0 coordinates; (2) number of epochs; (3) minimum peak Gaussian brightness temperature; (4) peak Gaussian brightness temperature at 25% of distribution; (5) median peak Gaussian brightness temperature; (6) peak Gaussian brightness temperature at 75% of distribution; (7) maximum peak Gaussian brightness temperature; (8) variability index of Gaussian brightness temperature; (9) number of robust speeds meeting criteria described in Section 2.2; (10) fastest apparent speed; (11) median apparent speed; and (12) apparent speed of feature that is closest to the core in its first measured epoch.

^a Lower limit value ($z = 0$) only on account of unknown source redshift.

(This table is available in its entirety in machine-readable form.)

and these values are tabulated in Table 3 with their distributions illustrated in Figure 4 and discussed in Section 3.1.2. We note that several brightness temperatures listed in the table are lower limits due only to the missing redshift information required for Equation (1) and are marked accordingly. These limits are computed assuming $z = 0$; however, the corresponding variability index, $V_{75,25}$, is not a lower limit as the redshift dependence cancels out.

2.2. Comparing Brightness Temperatures and Apparent Motions

As described in Section 1, the observed brightness temperature in the frame of the host galaxy is the intrinsic brightness temperature boosted by the Doppler factor: $T_{b,\text{obs}} = \delta T_{b,\text{int}}$. The unknown Doppler factor, $\delta = 1/[\Gamma(1 - \beta \cos \theta)]$, depends on the intrinsic flow speed, β , and angle to the line of sight, θ , in a similar fashion to the observed superluminal motion, $\beta_{\text{obs}} = \beta \sin \theta / (1 - \beta \cos \theta)$.

Our approach in this section is to compare a characteristic observed brightness temperature for each jet to its characteristic observed speed, following Homan et al. (2006). This comparison will allow us to find a typical intrinsic brightness temperature, $T_{b,\text{int}}$, for our sample as a whole. We will then take the analysis of Homan et al. (2006) a step further and use $T_{b,\text{int}}$ to estimate the Doppler factor, δ , for each individual jet. Combined with that jet’s observed speed, β_{obs} , we determine its Lorentz factor, Γ , and angle to the line of sight, θ .

2.2.1. Selecting Characteristic Values of Apparent Brightness Temperature and Kinematics

Homan et al. (2006) used the 25% point in the brightness temperature distribution of a given source as its characteristic brightness temperature; however, that choice was driven by the desire to avoid too many lower limits in a relatively small set of brightness temperature measurements available at the time. Our new data set is far larger, both in terms of numbers of epochs on individual sources and for the number of sources in our sample as

whole. Consequently we now simply use the median brightness temperature of a given source as its characteristic brightness temperature. Only those jets that have a median T_b value, not a limit, are used in the analysis. Limits are ambiguous in the statistical comparison and do not allow robust estimates of the relativistic properties. Fortunately only twelve of the 321 sources with viable observed speeds have median brightness temperature limits, and none of them are part of the MOJAVE 1.5 Jy QC flux-density-limited subsample.

In addition to summarizing the brightness temperature properties of each AGN jet, Table 3 also includes a summary of the distribution of apparent speed of features reported in MOJAVEXVIII. For characterizing the speed distribution of a given source, we only consider features with significant motions, $\geq 3\sigma$, in the approaching jet and discard those features identified as “inward” moving in MOJAVEXVIII. For each source, Table 3 reports the number of measured speeds, N_s , which meet these criteria and lists the maximum apparent speed, median apparent speed, and speed of the feature that was closest to the VLBI core in its first measured epoch. Unlike MOJAVEXVIII, which required at least five robust features to identify a median speed, here we report a fastest, median, and closest speed for every jet with at least one motion meeting the criteria described above.

In our previous papers we have taken the fastest observed speed in a given jet as the most representative of the underlying flow (e.g., Lister et al. 2009, 2019); however, the range of speeds in a source with many moving features can span a factor of a few, often including some very slow features. Jets with at least five features meeting our criteria have a median speed that is, on average, about 60% of the magnitude of their maximum observed speed. Because the features we observe may be propagating shocks (e.g., Marscher & Gear 1985; Hughes et al. 1989), they may travel at a different speed than the flow itself and the best observed speed to use in representing the flow remains an open question. To address this issue we directly compare three different choices for characterizing the observed speed of a jet to the median

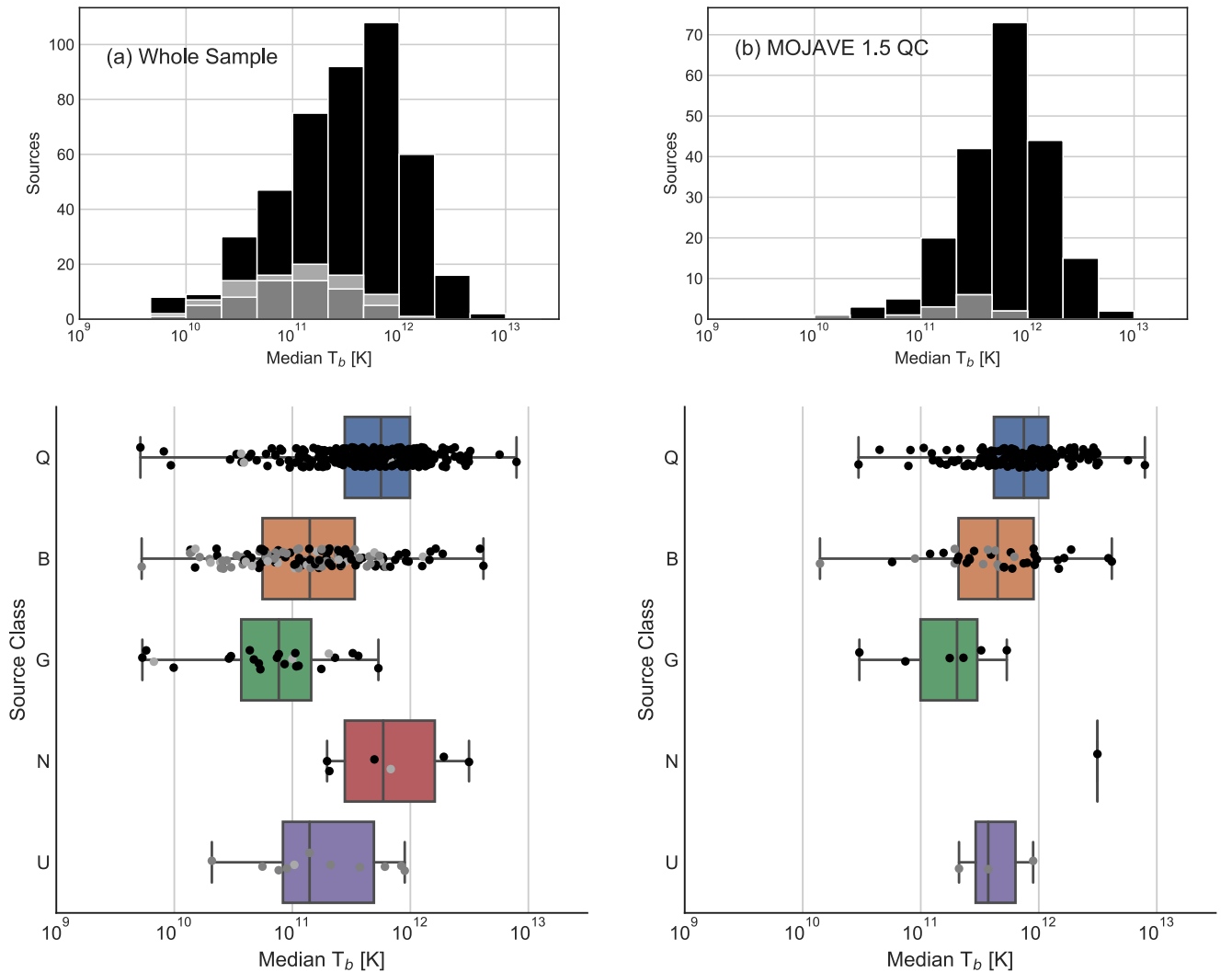


Figure 3. Distributions of median values of the measured Gaussian peak brightness temperatures for each source in the frame of the host galaxy. The upper panels are histograms, and the lower panels are combined box and scatter plots that break down the distributions by optical class where “Q” = quasars, “B” = BL Lacs, “G” = radio galaxies, “N” = narrow-line Seyfert Is, and “U” = unidentified. The filled regions of the box plots show the interquartile range, while the whiskers show the full extent of the data. Individual data points are shown as a scatter plot over the box plot to better illustrate the range and density of the data. Note that the interquartile range in each boxplot is shown without regard to limit status of the individual points; however, the overplotted points are marked as measurements or limits as described below. In running statistical tests between distributions, we use the log-rank test, as described in the text, to properly account for the limits. Gray filling indicates lower limits on the measured brightness temperature, where dark gray is for sources where the lower limit is solely due to the missing redshift. Panels on the left are for the entire source sample, while panels on the right contain just the flux-density-limited MOJAVE 1.5 Jy QC sample.

observed brightness temperature of the jet cores for those sources with several moving features, $N_s \geq 5$.

Figure 5 compares median brightness temperature of the core with the fastest observed speed, β_{\max} , the median speed, β_{med} , and the speed of the feature closest to the core, β_{close} . The same 83 jets with at least five moving features are shown in each panel; the only difference is the speed used to represent each jet on the y-axis. The strongest correlation with median T_b is for the fastest apparent speed (see panel (a)) with a Spearman $\rho = 0.63$, while the median and closest features have $\rho = 0.58$ and $\rho = 0.36$ respectively. It is important to note that even with ideal measurements, we do not expect a perfect correlation between the observed brightness temperature and apparent speed. At the “critical” angle that maximizes apparent superluminal motion with $\cos \theta = \beta$,

$$\beta_{\text{obs}} = \beta \delta = \beta T_{\text{b,obs}} / T_{\text{b,int}}, \quad (3)$$

which would indeed suggest a strong correlation given that β is typically very nearly unity for powerful AGN jets; however, some jets may lie at smaller or larger angles than the critical angle and consequently have larger or smaller Doppler factors respectively. Indeed we will see this effect below when we look at the full data set; however, this subset of 83 jets includes only those that have at least five moving features meeting the criteria outlined above. Jets where we can identify and follow several moving features may be more likely to be near the critical angle where we are viewing the jet structures from the side in the comoving frame, and the strong correlation seen in panel (a) is consistent with that expectation. In our view, the fastest observed speed, β_{\max} , is the best speed to use in comparing to core brightness temperatures across the sample, and we use β_{\max} in the analysis that follows. In Section 3.2.2, we revisit this question in the light of possible jet acceleration and

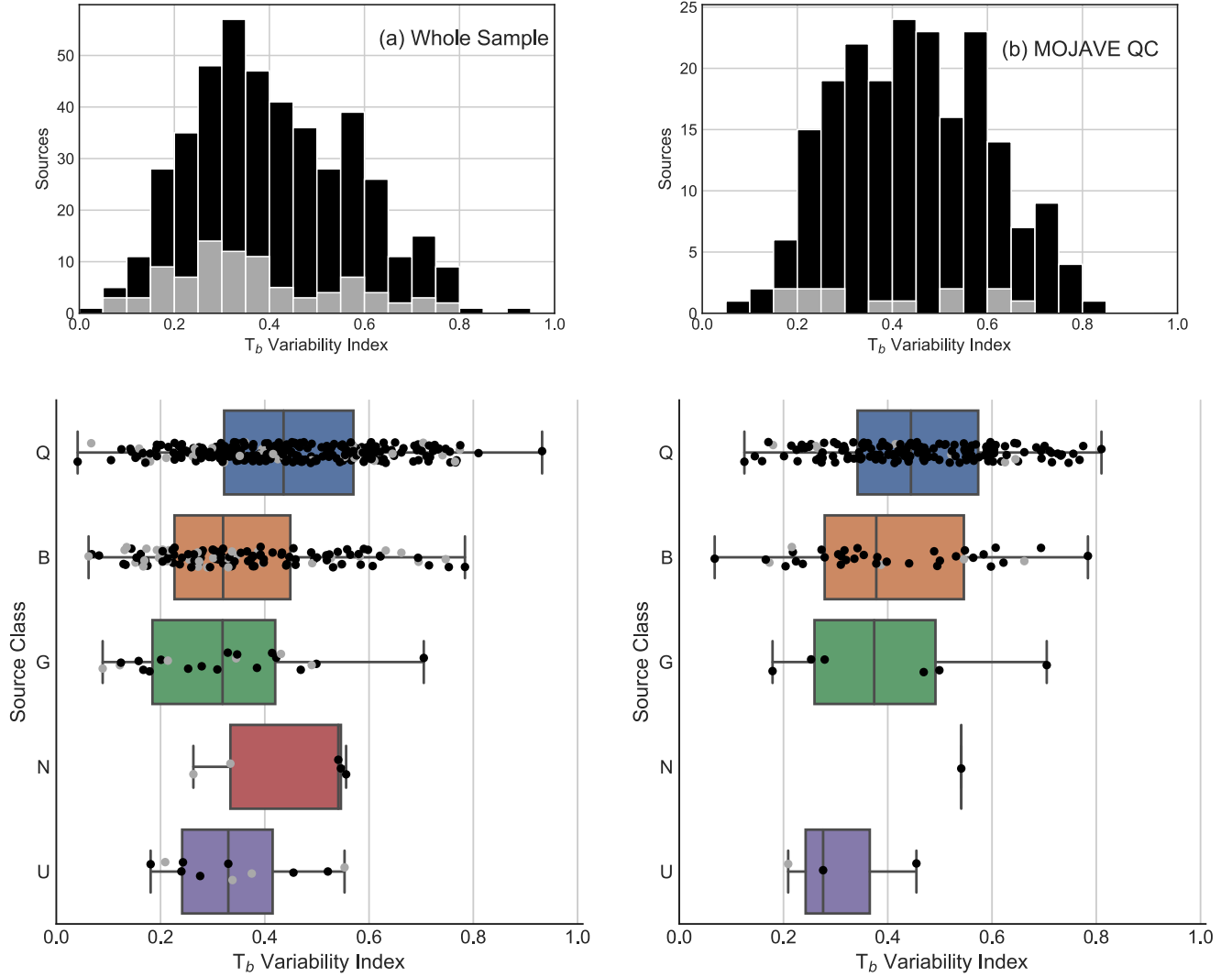


Figure 4. Distributions of the brightness temperature variability index for each source. The upper panels are histograms, and the lower panels are combined box and scatter plots that break down the distributions by optical class where “Q” = quasars, “B” = BL Lacs, “G” = radio galaxies, “N” = narrow-line Seyfert Is, and “U” = unidentified. The filled regions of the box plots show the interquartile range, while the whiskers show the full extent of the data. Individual data points are shown as a scatter plot over the box plot to better illustrate the range and density of the data. Note that the interquartile range in each boxplot is shown without regard to limit status of the individual points; however, the overplotted points are marked as measurements or limits as described below. In running statistical tests between distributions, we use the log-rank test, as described in the text, to properly account for the limits. Gray filling indicates lower limits on the variability index. Panels on the left are for the entire source sample, while panels on the right contain just the flux-density-limited MOJAVE 1.5 Jy QC sample.

consider the effects on our results if the median speed is used instead.

2.2.2. Estimating the Typical Median Intrinsic Brightness Temperature

In a complete, flux-density-limited sample, jets are more likely to be observed at a smaller angle to the line of sight than the critical angle due to Doppler beaming selection (e.g., Cohen et al. 2007). Lister & Marscher (1997) found that a typical beamed jet in a flux-density-limited sample like the MOJAVE 1.5 Jy QC sample has an angle to the line of sight about one-half of the critical angle, and Homan et al. (2006) used a simulation of a flux-density-limited sample to estimate that about 75% of the jets should lie inside the critical angle with a Doppler beaming factor:

$$\delta > \sqrt{1 + \beta_{\text{obs}}^2} \simeq \beta_{\text{obs}}. \quad (4)$$

To update this estimate, we created 1000 Monte Carlo simulations of a 174-source, flux-density-limited sample based on the parameters estimated by Lister et al. (2019), and we find that 69% of the simulated jets lie within the critical angle. While the full results of the Monte Carlo simulation reported in that paper are based on the luminosities and apparent speeds of the MOJAVE 1.5 Jy QC quasars at that time, in this work we only use the fraction of simulated jets within the critical angle to allow us to estimate the typical median intrinsic brightness temperature, $T_{\text{b,int}}$, of our sample as a whole.

Following Homan et al. (2006) we start by assuming that every source in our sample has the same median intrinsic brightness temperature, and therefore that any differences in observed median brightness temperatures between sources are due to their Doppler beaming factor. With this assumption we can calculate the expected observed median brightness temperature for jets at the critical angle: $T_{\text{b,obs}} = \sqrt{1 + \beta_{\text{obs}}^2} T_{\text{b,int}}$. Jets with larger observed

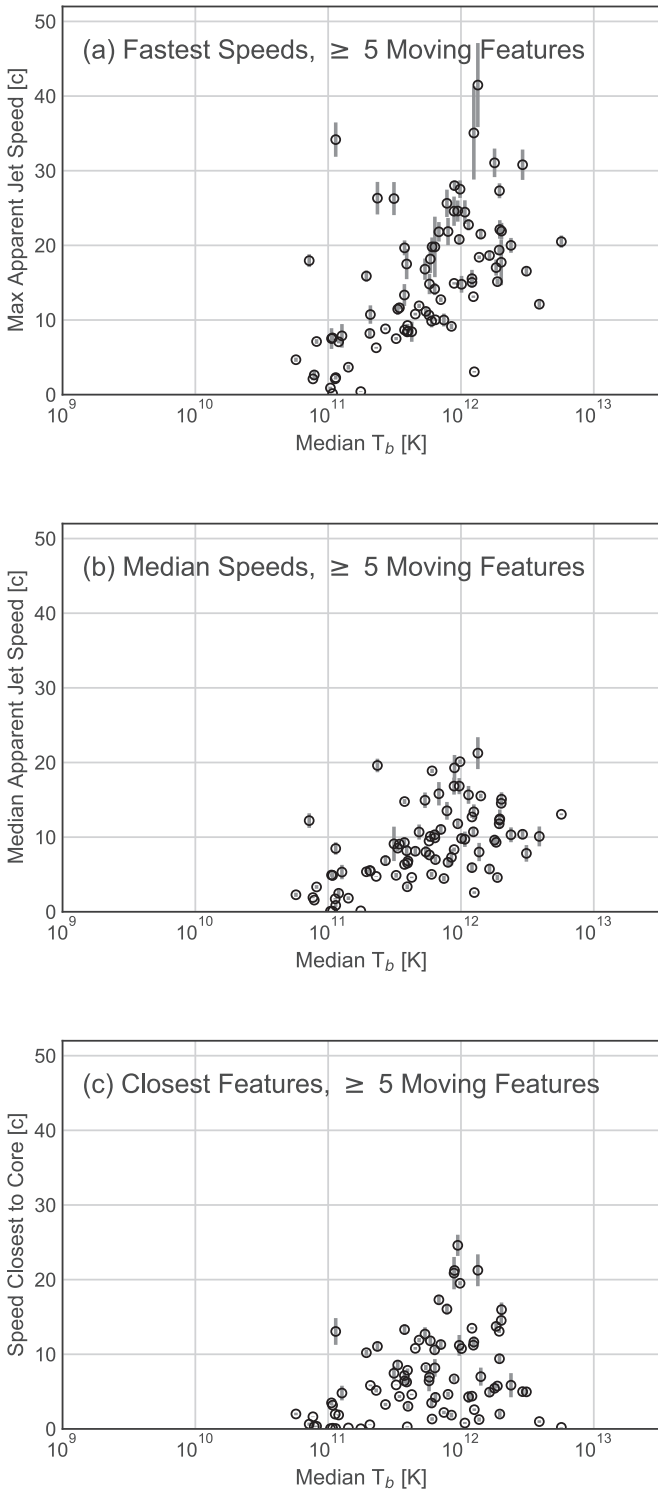


Figure 5. Apparent speed vs. median Gaussian brightness temperature in the core for all 83 sources with ≥ 5 moving features meeting the criteria described in Section 2.2. Panels (a), (b), and (c) show respectively the fastest speed, median speed, and speed found closest to the core region. The fastest apparent speeds have the strongest correlation with the median brightness temperature of the core.

median brightness temperatures are therefore more highly beamed and located inside the critical angle. We vary $T_{b,int}$ until 69% of our sample lie inside the critical angle.

There are 178 sources in the MOJAVE 1.5 Jy QC sample with both observed median brightness temperatures and

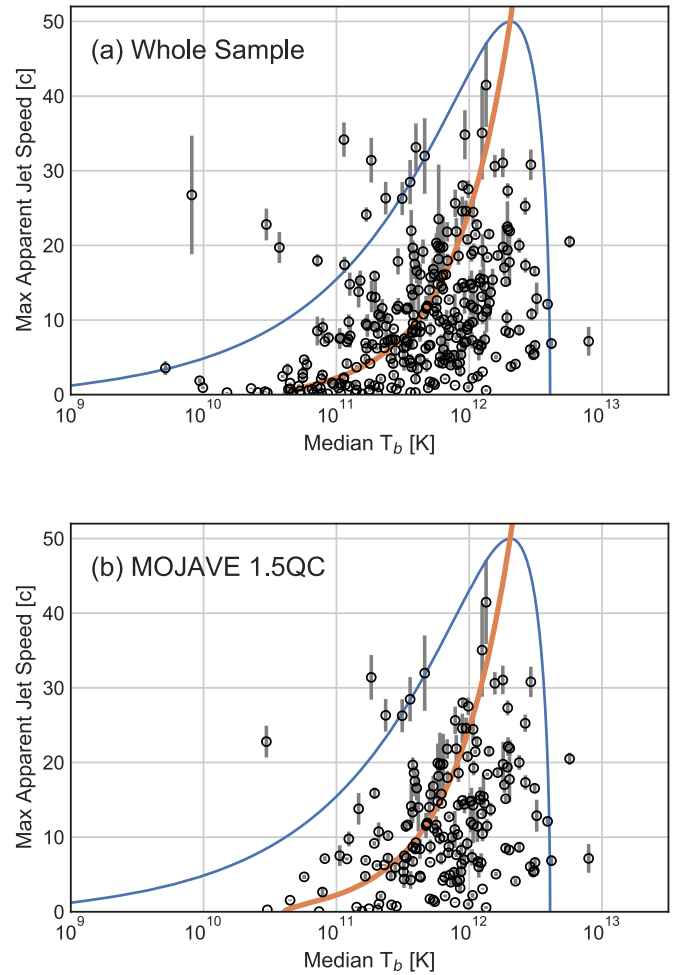


Figure 6. Apparent speed vs. median Gaussian brightness temperature in the core. Panel (a) includes all 309 sources with apparent speeds and median brightness temperature measurements, and panel (b) includes just the 178 sources from the MOJAVE 1.5 Jy QC sample. Each panel has two curves. The first curve is a red-orange line through the center of the plot, which shows where sources with intrinsic brightness temperature = $10^{10.609}$ K, would fall if viewed at the critical angle, $\cos \theta = \beta$. The second curve is a blue “envelope,” which shows where sources with a Lorentz factor of 50 would fall if seen at the full range of angles to the line of sight.

observed speeds, 149 of which are quasars. Using the whole 1.5 Jy QC sample, we find the best estimate for the median intrinsic brightness temperature to be $T_{b,int} = 10^{10.609}$ K, and restricting the sample to only quasars does not change this value appreciably. We estimate the uncertainty in this value in two ways: (1) by creating 10,000 samples of 178 sources by randomly drawing with replacement from the data itself to include the effects of a limited sample size; and (2) by changing our fraction of sources within the critical angle by $\pm 5\%$ and repeating this estimate using 64% and 74% of sources within the critical angle. Including these uncertainties, our best estimate for the typical median intrinsic brightness temperature of the sample is $T_{b,int} = 10^{10.609 \pm 0.067}$ K = $4.1(\pm 0.6) \times 10^{10}$ K.

Figure 6 shows plots of maximum observed jet speeds versus observed median brightness temperature for both our entire sample (panel (a)) and for the MOJAVE 1.5 Jy QC sample (panel (b)). The superimposed lines use our estimated value for the intrinsic median brightness temperature. The first curve is a red-orange line through the center of the plot, which shows where jets with intrinsic brightness temperature = $10^{10.609}$ K

Table 4
Doppler Factors and Derived Properties

Source	$T_{b,\text{med}}$ (\log_{10} K)	β_{max}	δ	Γ	θ (deg)	θ_{src} (deg)
(1)	(2)	(3)	(4)	(5)	(6)	(7)
0003+380	11.550	4.61 ± 0.36	8.7	5.6	5.5	56.1
0003-066	11.079	7.08 ± 0.21	3.0	10.1	13.8	135.4
0006+061	>11.021	...	>2.6
0007+106	11.729	1.58 ± 0.29	13.2	6.7	1.0	13.7
0010+405	>11.425	6.92 ± 0.64	>6.5
0011+189	>11.207	4.54 ± 0.46	>4.0
0012+610	>10.747 ^a	...	>1.4
0014+813	11.223	9.47 ± 0.91	4.1	13.1	10.2	133.5
0015-054	11.246	...	4.3
0016+731	11.902	7.64 ± 0.32	19.6	11.3	2.0	42.6
...						

Notes. The complete version of this table appears in the online journal. Table of source properties deduced from the brightness temperature versus speed analysis. All 447 sources are included in this table, but only 309 sources have both measured apparent speeds and non-limit-brightness temperatures, making them suitable for the full analysis as described in Section 2.2. Columns are as follows: (1) source name in B1950.0 coordinates; (2) median peak Gaussian brightness temperature; (3) fastest apparent speed; (4) Doppler factor, assuming $T_{b,\text{int}} = 10^{10.609}$ K as found in Section 2.2; (5) Lorentz factor derived from δ and β_{max} ; (6) angle to the line of sight derived from δ and β_{max} ; and (7) angle to the line of sight in the comoving jet frame.

^a Lower limit value ($z = 0$) only on account of unknown source redshift.

(This table is available in its entirety in machine-readable form.)

would fall if viewed at the critical angle, $\cos \theta = \beta$. The second curve is a blue “envelope,” which shows where jets with the same intrinsic brightness temperature and a Lorentz factor of 50 would fall if seen at the full range of angles to the line of sight. If all of the jets in our sample have this same median intrinsic brightness temperature, jets with Lorentz factors < 50 should fall below the blue curve, and jets viewed inside the critical angle should fall to the right of the red-orange curve.

2.2.3. Finding δ , Γ , and θ

For each source in our sample, we use the assumption that they all have the same intrinsic median brightness temperature found above, $T_{b,\text{int}} = 10^{10.609 \pm 0.067}$ K, to estimate their Doppler factor from their median observed brightness temperature, $\delta = T_{b,\text{obs}}/T_{b,\text{int}}$. We then use their maximum observed speeds, β_{max} , to find their Lorentz Factor, Γ , angle to the line of sight, θ , and angle to the line of sight in the source fluid frame, θ_{src} , as follows, e.g., Jorstad et al. (2017):

$$\Gamma = (\beta_{\text{max}}^2 + \delta^2 + 1)/2\delta; \quad (5)$$

$$\theta = \arctan \frac{2\beta_{\text{max}}}{\beta_{\text{max}}^2 + \delta^2 - 1}; \quad (6)$$

$$\theta_{\text{src}} = \arccos \frac{\cos \theta - \beta}{1 - \beta \cos \theta}. \quad (7)$$

These values are listed in Table 4, with distributions of δ , Γ , and θ shown in Figure 7.

2.2.4. Comparing Doppler Factor Values to Previous Estimates

It is interesting to compare Doppler factors we estimated from the median core brightness temperature to the values obtained by different methods. Doppler factors have been

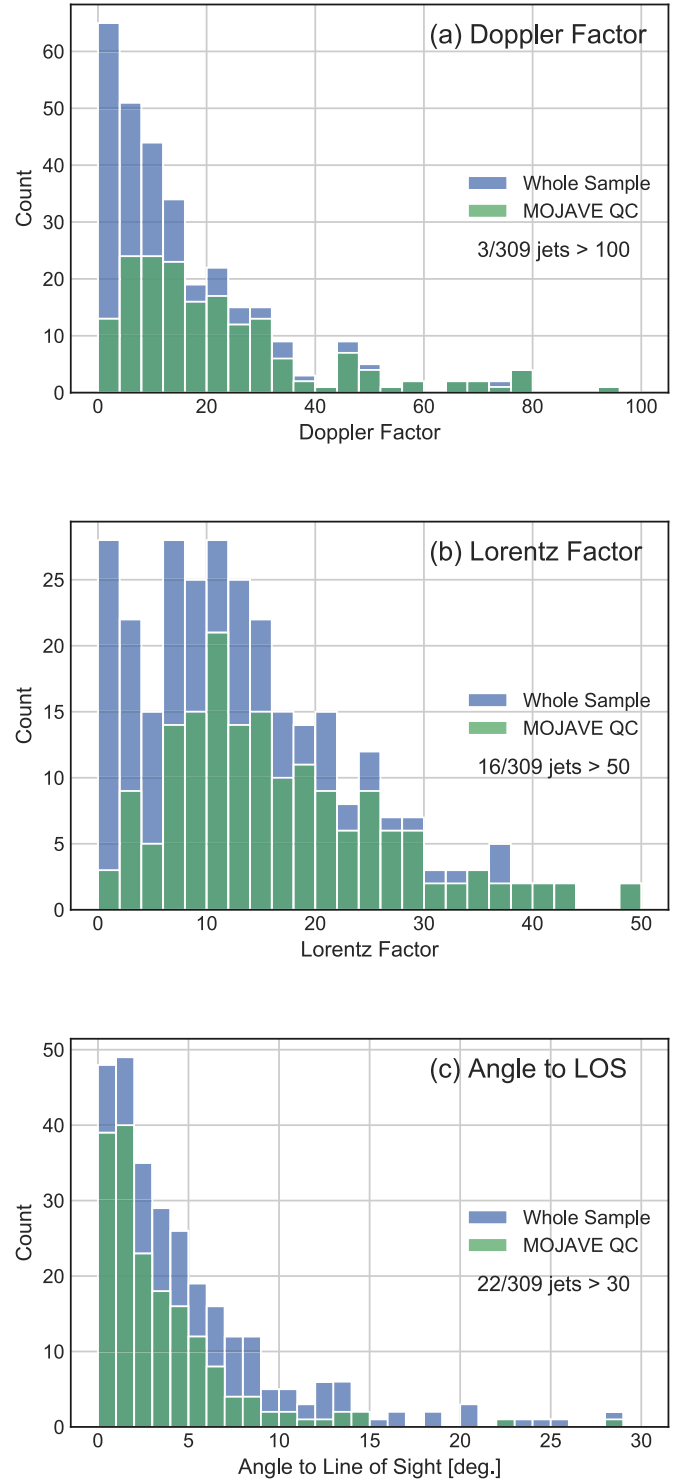


Figure 7. Histograms of Doppler factor, δ , Lorentz Factor, Γ , and angle to the line of sight, θ , derived from the median brightness temperature and apparent speeds as described in Section 2.2.3. Note that a few outliers at larger values are not included on the plots for readability and the number of these are indicated on each panel.

estimated for a large number of sources by flare modeling using the data of the single-dish monitoring programs at the OVRO 40 m radio telescope at 15 GHz (Lioudakis et al. 2018), at the Metsähovi Radio Observatory at 22 and 37 GHz (Hovatta et al. 2009), and at the Effelsberg 100 m and IRAM 30 m telescopes within the F-GAMMA project at the frequencies from 2.64 to

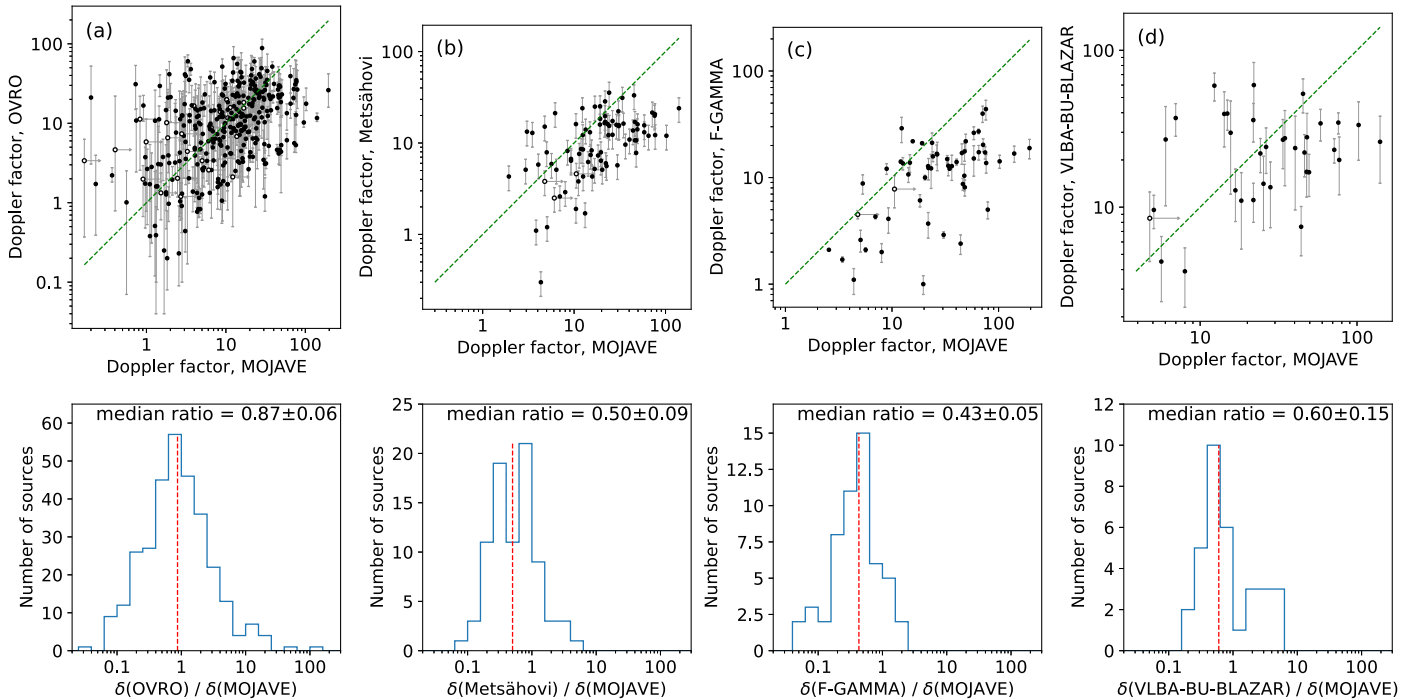


Figure 8. Comparison of the Doppler factors estimated in this work with those previously estimated from different monitoring programs: (a) OVRO (Liodakis et al. 2018); (b) Metsähovi (Hovatta et al. 2009); (c) F-GAMMA (Liodakis et al. 2017); (d) VLBA-BU-BLAZAR (Jorstad et al. 2017). Upper panel: our measured values are marked by dots, while our lower limits are marked by open circles with arrows. The dashed line marks the ideal case when Doppler factors are equal. Lower panel: distributions of the ratio of the Doppler factors. The median ratios are marked by vertical red dashed lines and are given above each histogram with their errors estimated by bootstrapping. See the discussion of the correlations and offsets in Section 2.2.4.

86 GHz (Liodakis et al. 2017). Jorstad et al. (2017) estimated Doppler factors by another method, using the flux-density decay timescale of VLBI superluminal components at 43 GHz. Figure 8 shows the comparison of these values with our results. There is a statistically significant correlation between our Doppler factors and those obtained from the single-dish monitoring programs (panels (a)–(c)): p -values determined by the Kendall partial (given redshift) correlation test, accounting also for lower limits, are no more than 10^{-3} .

The most significant correlation, $p \approx 10^{-12}$, is with the OVRO values (Figure 8(a), upper panel). These values also have the smallest median offset, about 10%, from our estimates (Figure 8(a), lower panel). The Doppler factors presented here and in the OVRO results are estimated by two very different methods, in different states of the sources with quite different corresponding estimates for $T_{b,int}$ in those states. As described in Section 3.3, our typical intrinsic core brightness temperature for the median state is at or below the equipartition value while the flaring state intrinsic core brightness temperature from Liodakis et al. (2018) is only 2 times smaller than the inverse Compton limit (Kellermann & Pauliny-Toth 1969; Readhead 1994). The fact that the resulting Doppler factors are in such a good agreement lends confidence to both methods, although we note that the two approaches are not totally independent as Liodakis et al. (2018) used population modeling of an earlier set of MOJAVE kinematics to help constrain their value of $T_{b,int}$ in the flaring state.

The values from Hovatta et al. (2009) and Liodakis et al. (2017) also correlate with ours, but are, on average, about two times smaller (Figures 8(b) and (c)). In both of these works, the authors used as intrinsic brightness temperature its equipartition value $T_{eq} = 5 \times 10^{10}$ K (Readhead 1994). Re-scaling their Doppler factors to the higher $T_{b,int} = 2.8 \times 10^{11}$ K value used by Liodakis

et al. (2018) would decrease them by about a factor of two, increasing their difference from our estimates. Liodakis et al. (2018) discuss several possible reasons for this disagreement between the otherwise similar variability approaches, including possibly insufficient cadence of the earlier observations. Our Doppler factors and those from Jorstad et al. (2017) are poorly correlated, regardless of which Doppler factor values for individual jet components from Jorstad et al. (2017) are used to represent each source: the maximum, the median, or the average value. For Figure 8(d), the maximum values are used. The Doppler factors estimated by Jorstad et al. (2017) may simply have a larger scatter if the assumption that the observed flux density decay timescale of jet components equals their light-crossing time divided by the Doppler factor is not always satisfied.

3. Results and Discussion

3.1. Observed Brightness Temperature

In the frame of the host galaxy, the observed brightness temperature of the core of an AGN jet depends on both the Doppler boosting factor, δ , of the jet flow and the intrinsic brightness temperature, $T_{b,int}$ of the emission region: $T_{b,obs} = \delta T_{b,int}$. For an individual jet, observed changes in $T_{b,obs}$ can reflect changes in either quantity or both. The Doppler boosting factor can vary if there are changes in the flow speed or direction, and the intrinsic brightness temperature can change with optical depth (expected to be near unity in AGN jet cores) and the balance between particle and field energy in the emission region (e.g., Readhead 1994).

Our measurements of the Gaussian peak brightness temperature of the core region of each jet, in every epoch, are reported in Table 2 and illustrated in Figure 2. From studying individual sources in Figure 2, it is apparent that the typical variation in

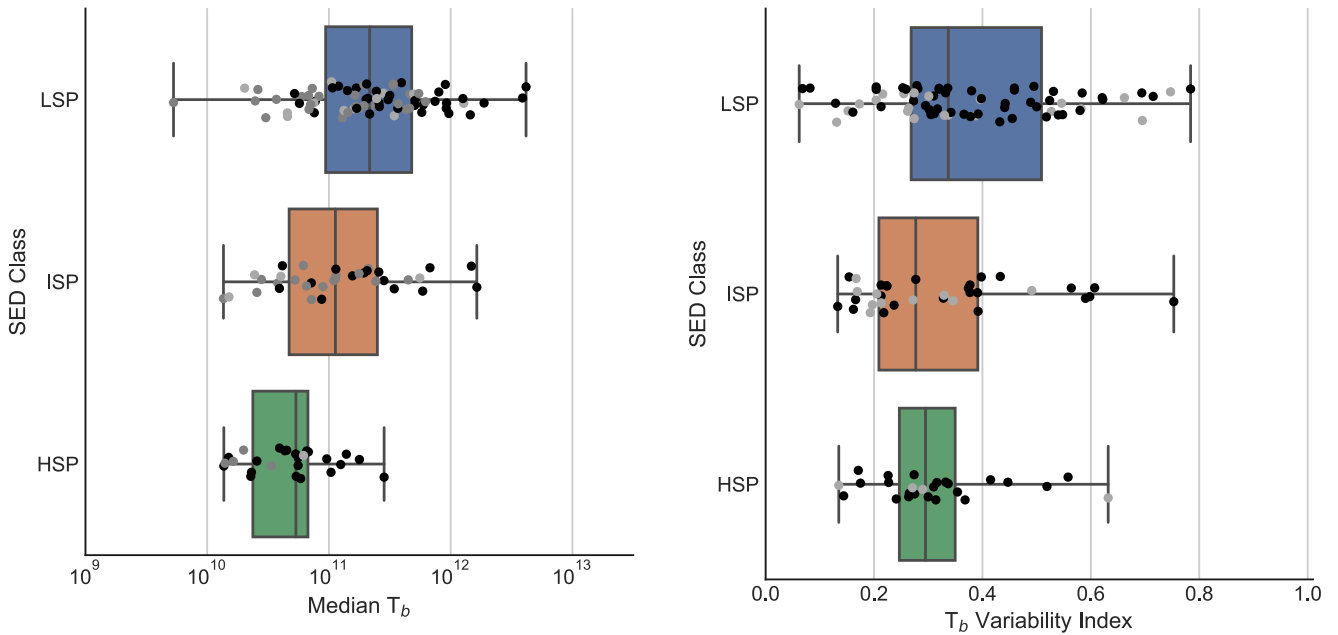


Figure 9. Distributions of the brightness temperature (left) and variability index (right) for the BL Lac objects in our whole sample as a function of SED Class. The “LSP,” “ISP,” and “HSP” abbreviations indicate low, intermediate, and high-synchrotron-peak sources respectively. The scattered points plotted over each box plot indicates the locations of the individual values for that distribution. Note that the interquartile range in each boxplot is shown without regard to limit status of the individual points; however, the overplotted points are marked as measurements or limits as described below. In running statistical tests between distributions, we use the log-rank test, as described in the text, to properly account for the limits. Gray filling indicates lower limits, where the darker gray is for sources where the lower limit is solely due to the missing redshift.

$T_{b,obs}$ over time for a given jet is a factor of a few up to about an order of magnitude, with a few extreme cases, like 0716 +714, having larger variations. However the differences between AGN can be much larger, with median brightness temperature values spanning up to three orders of magnitude across our heterogeneous 447-source sample. The flux-density-limited MOJAVE 1.5 Jy QC subsample has median brightness temperatures that span a somewhat narrower range of about two and half orders of magnitude, see Figure 3.

This range of observed median brightness temperatures is consistent with Doppler boosting being the primary difference between AGN jets in their median state; however, variations over time for an individual jet may be more strongly connected to the emergence of new features and changes in the energy balance between particles and magnetic fields in the emission region. In the subsections that follow, we look first at trends with median brightness temperature across the sample (Section 3.1.1), and we then consider variability in brightness temperature (Section 3.1.2).

3.1.1. Trends with Median T_b

Figure 3 showed histograms of the median observed brightness temperatures for our sample as a whole (panel (a)) and the MOJAVE 1.5 Jy QC subsample (panel (b)), and beneath these panels we showed box plots illustrating the range of median brightness temperature values for different optical classes. Quasars ($n_{ws} = 271$, $n_{m15} = 158$)¹⁵, BL Lacs ($n_{ws} = 136$, $n_{m15} = 37$), and galaxies ($n_{ws} = 23$, $n_{m15} = 6$) appear to differ in their median brightness temperatures. Because some of our median brightness temperatures are lower limits, we use a pair-wise log-rank test from the Numerical Python “lifelines” distribution

(Davidson-Pilon et al. 2020) to account for this censored data. We find that galaxies are very unlikely to be drawn from the same distribution as quasars ($p_{ws} < 0.001$, $p_{m15} < 0.001$) or BL Lacs ($p_{ws} < 0.001$, $p_{m15} < 0.001$). BL Lacs appear to differ from quasars for our whole sample ($p_{ws} = 0.028$) but we detect no difference in the flux-density-limited MOJAVE 1.5 Jy QC subsample ($p_{m15} = 0.93$).

The BL Lacs in our flux-density-limited, MOJAVE 1.5 Jy QC sample are strongly dominated by sources with a spectral energy distribution characterized by a low synchrotron peak (LSP). In Figure 9, we compare the median brightness temperatures of LSP BL Lacs ($n = 75$) to those with intermediate or high-synchrotron-peaked (HSPs), ISP ($n = 35$) and HSP ($n = 26$), which are better represented in our whole, heterogeneous sample. HSP BL Lacs have distinctly lower median brightness temperatures when compared to ISP or LSP BL Lacs as confirmed by a log-rank test with $p < 0.001$ for both comparisons; however, we detect no difference between the median brightness temperature distributions of ISP and LSP BL Lac classes ($p = 0.14$). Figure 10 shows a plot of SED peak frequency in the galaxy rest frame versus median brightness temperature. BL Lac objects in particular show a strong negative correlation between SED peak frequency and median brightness temperature.

If the median observed brightness temperature is a good proxy for the Doppler beaming factor, these results mean that radio galaxies are less beamed than BL Lacs and quasars as one would expect from unification arguments (e.g., Urry & Padovani 1995); however, we do not detect a difference between BL Lacs and quasars in the flux-density-limited MOJAVE 1.5 Jy QC sample. The apparent difference between these two classes in our larger, heterogeneous sample is likely due to differences within the BL Lac optical class itself. The differences in median brightness temperature between HSP and LSP sources suggest that HSP BL Lacs are less beamed than those whose SEDs peak at lower

¹⁵ The subscript “ws” refers to our whole sample, while “m15” is the MOJAVE 1.5 Jy QC flux-density-limited subsample.

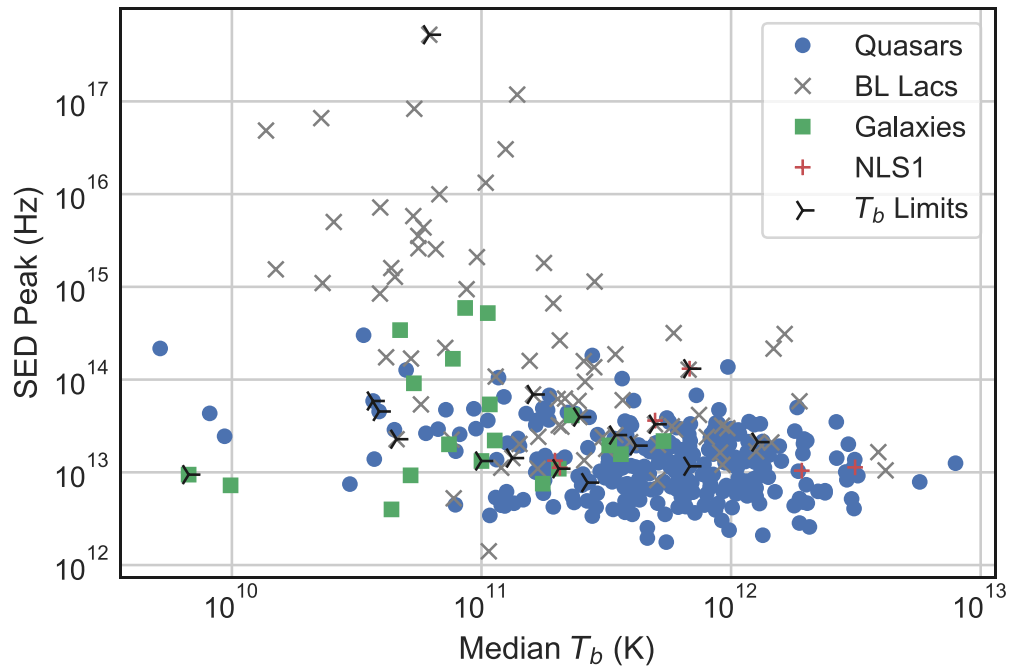


Figure 10. Spectral energy density peak frequency in the host galaxy rest frame vs. median Gaussian brightness temperature for the whole sample.

frequencies, consistent with earlier findings (e.g., Nieppola et al. 2008; Lister et al. 2011).

In Figure 11 we plot γ -ray luminosity versus median brightness temperature for 291 Fermi/LAT-detected AGN. The luminosity values are computed from the Fermi/LAT 10 yr point-source catalog (Ajello et al. 2020) using their 0.1–100 GeV energy flux and power-law spectral index following the approach given by Lister et al. (2011), Equation (3). To allow computation of their luminosity and to avoid issues related to galactic foreground subtraction, only sources with known redshifts and with a galactic latitude $|b| > 10^\circ$ are included in this plot. The histogram at the bottom of the plot shows the 60 sources meeting the same criteria that do not have Fermi/LAT detections in the 10 yr point-source catalog.

We see a strong, positive correlation between γ -ray luminosity and median observed brightness temperature. Figure 11 includes lower limits on the median brightness temperature of only 13/291 of our LAT-detected AGN, and we measure a significant Spearman rank correlation for the remaining 278 sources of $\rho = 0.54$ ($p < 0.001$). However, we must be cautious in interpreting this correlation, as selection effects must be considered as well as common factors that affect both T_b and the γ -ray luminosity.

The observed brightness temperature in the frame of the host galaxy depends only weakly on redshift, see Equation (1), and even if we divide out the factor of $(1+z)$, the correlation remains significant ($\rho = 0.32$, $p < 0.001$). Another possible confounding factor is that many sources in our sample are selected on the basis of their radio flux density as part of the flux-density-limited MOJAVE 1.5 Jy QC subsample, and sources at large distances are likely to be highly beamed to meet this criterion, creating a natural correlation between Doppler factor and luminosity distance. In this same group of 278 sources we find a correlation of $\rho = 0.44$ ($p < 0.001$) between median brightness temperature and luminosity distance squared, D_L^2 . If we divide the γ -ray luminosity by D_L^2 , the correlation with median brightness temperature still remains significant with $\rho = 0.33$ ($p < 0.001$).

We can test the relationship between median brightness temperature and γ -ray emission further by comparing these results to those of Kovalev et al. (2009) and Lister et al. (2011) who found that γ -ray detected jets in earlier LAT catalogs had higher brightness temperatures than non-detected jets. Here we use a log-rank test to compare the distributions of median brightness temperature of the detected γ -ray sources ($n = 291$) to the non-detected sources ($n = 60$) in Figure 11, and we find the two groups are very unlikely to be drawn from the same distribution ($p < 0.001$) with the detected sources having distinctly larger median brightness temperatures on average. The Log-Rank test correctly accounts for the lower limits on some of our brightness temperature values, and by simply comparing the detected versus non-detected distributions we are not biased by a possible luminosity distance correlation with median brightness temperature through our flux-density-limited radio sample.

Taken together these results imply a common Doppler boosting of both the γ -ray emission and the brightness temperature of the radio core and will be discussed further in Section 3.2.1.

3.1.2. T_b Variability

As described in Section 2.1, we characterize the brightness temperature variability of each jet by using a fractional measure of the variability between the 25% and 75% points in the brightness temperature distribution over time, see Equation (2). Figure 4 showed histograms of this brightness temperature variability index for our whole sample (panel (a)) and the MOJAVE 1.5 Jy QC subsample (panel (b)). Box plots below each histogram showed the distribution of variability index for different optical classes. Across the whole sample, quasars ($n = 269$)¹⁶ appear to have higher variability and a log-rank test confirms that their distribution differs significantly from both BL Lacs ($n = 132$, $p = 0.006$) and radio galaxies ($n = 22$,

¹⁶ The number of sources with valid variability index values may be smaller than the number with brightness temperature measurements due to ambiguous combinations of lower limits in some cases.

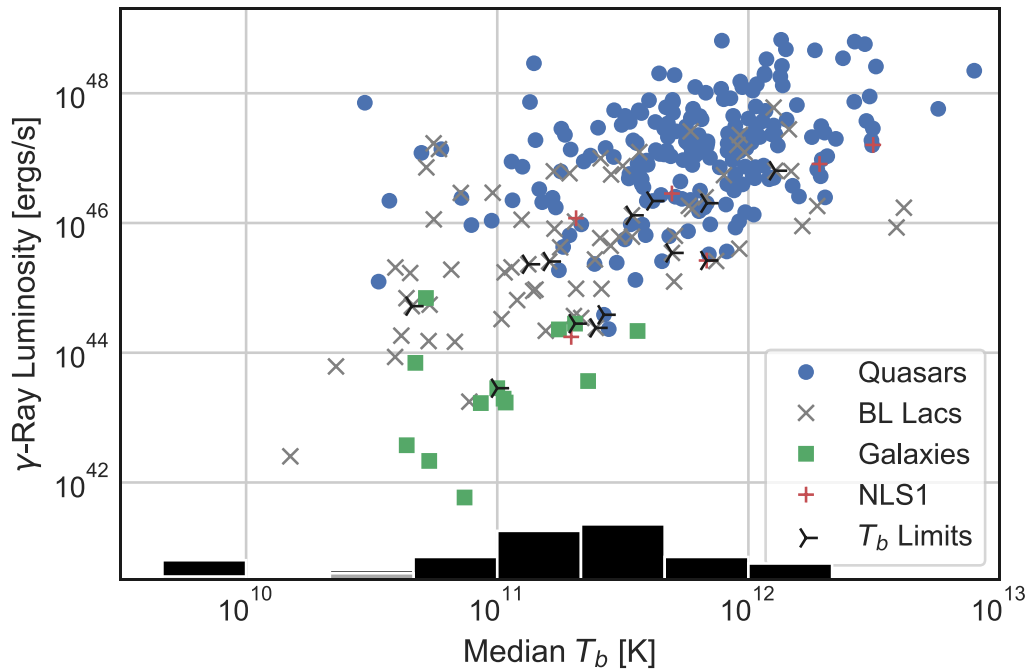


Figure 11. γ -ray luminosity vs. median Gaussian brightness temperature for 291 Fermi/LAT-detected AGN. The histogram at the bottom of the plot shows the distribution of 60 sources in our sample with measured brightness temperature but without Fermi/LAT detections, gray bars in the histogram indicate lower limits on the measured brightness temperature. Only sources with known redshifts and with a galactic latitude $|b| > 10^\circ$ are included in this plot.

$p = 0.011$), although we detect no difference between BL Lacs and radio galaxies when compared to each other ($p = 0.36$). For the MOJAVE 1.5 Jy QC flux-density-limited sample, we are unable to detect any difference in variability index distributions between quasars ($n = 158$), BL Lacs ($n = 37$), and radio galaxies ($n = 6$) with $p \geq 0.48$ for each paired comparison.

The right panel of Figure 9 showed box plots of the brightness temperature variability index of ISP ($n = 71$), LSP ($n = 35$), and HSP ($n = 26$) BL Lacs in our sample as a whole, and paired log-rank tests show that HSP and LSP BL Lacs differ significantly from each other ($p = 0.004$); however, we do not detect differences from ISP BL Lacs for either of them ($p = 0.18$ versus LSP and $p = 0.21$ versus HSP).

3.2. Doppler Factors and Intrinsic Jet Properties

In Section 2.2 we compared median observed brightness temperatures of jet cores in the host galaxy frame to the maximum apparent speeds in their jets to find a single, typical intrinsic brightness temperature, $T_{b,int} = 10^{10.609 \pm 0.067}$ K, which we could apply to estimate Doppler factors from the median observed brightness temperature of each source: $\delta = T_{b,obs}/T_{b,int}$. Combined with our apparent speed measurements, we estimated Lorentz factors, angles to the line of sight, and angles to the line of sight in the source fluid frame (θ_{src}) for 309 sources for which we had all the necessary information, 178 of which are in the MOJAVE 1.5 Jy QC flux-density-limited sample.

Histograms of δ , Γ , and θ for those sources where we have estimates for all three quantities were shown in Figure 7. For the MOJAVE 1.5 Jy QC sample, the overall trend and shape in these histograms is similar to the simulated Monte Carlo distribution discussed by Lister et al. (2019, Figure 11). The latter was fitted using the observed redshift, 15 GHz flux density, and apparent jet speed distributions reported in that paper for the 1.5 Jy QC sample. Our Doppler factor distribution

peaks near $\delta = 10$ and has a long, shallow tail out to 100, with just three jets beyond that point. We also see that the Lorentz factor distribution peaks near $\Gamma = 10$, with a slower fall off toward $\Gamma = 50$ and eight sources from the flux-density-limited sample at larger values. For the angle to the line of sight, we do not see the sharp decline toward $\theta = 0^\circ$ from the simulation, likely due to the uncertainty in our Doppler factor estimates described below, but our viewing angle distribution does peak between 1° and 2° , with a sharp decline out to 10° and beyond, similar to the simulation. It is important to note that while we did not fit to the Lister et al. (2019) simulation in a detailed way, our procedure for estimating the best value for $T_{b,int}$ did seek to match the fraction of simulated sources inside the critical angle for superluminal motion.

Our analysis assumes that a single value of $T_{b,int}$ applies to all jets in their median state, and while this assumption seems to do a reasonable job estimating the Doppler factors of jets in our population, there may be some natural spread in this value. Sources with intrinsically smaller or larger values of $T_{b,int}$ would then appear to have corresponding larger or smaller Doppler factors in our data, leading to a blurring of our Doppler factor distribution. We estimate this effect, along with any other uncertainties that can lead to spread in our data, by comparing the distribution of Doppler factors in the Lister et al. (2019) simulation with the corresponding quantity from the quasars in our flux-density-limited sample. The distribution from the simulation is narrower than the one that is derived from the median $T_{b,obs}$ values, and by comparing the standard deviation of the logarithms of the two distributions, we can estimate the additional spread in the measured distribution. In this way we estimate our Doppler factors are good to, i.e., have a 1σ spread of, a multiplicative factor of approximately 1.8.¹⁷

¹⁷ Despite the numerical coincidence, this factor is unrelated to the 1.8 geometric conversion factor for brightness temperatures discussed in Section 2.1.

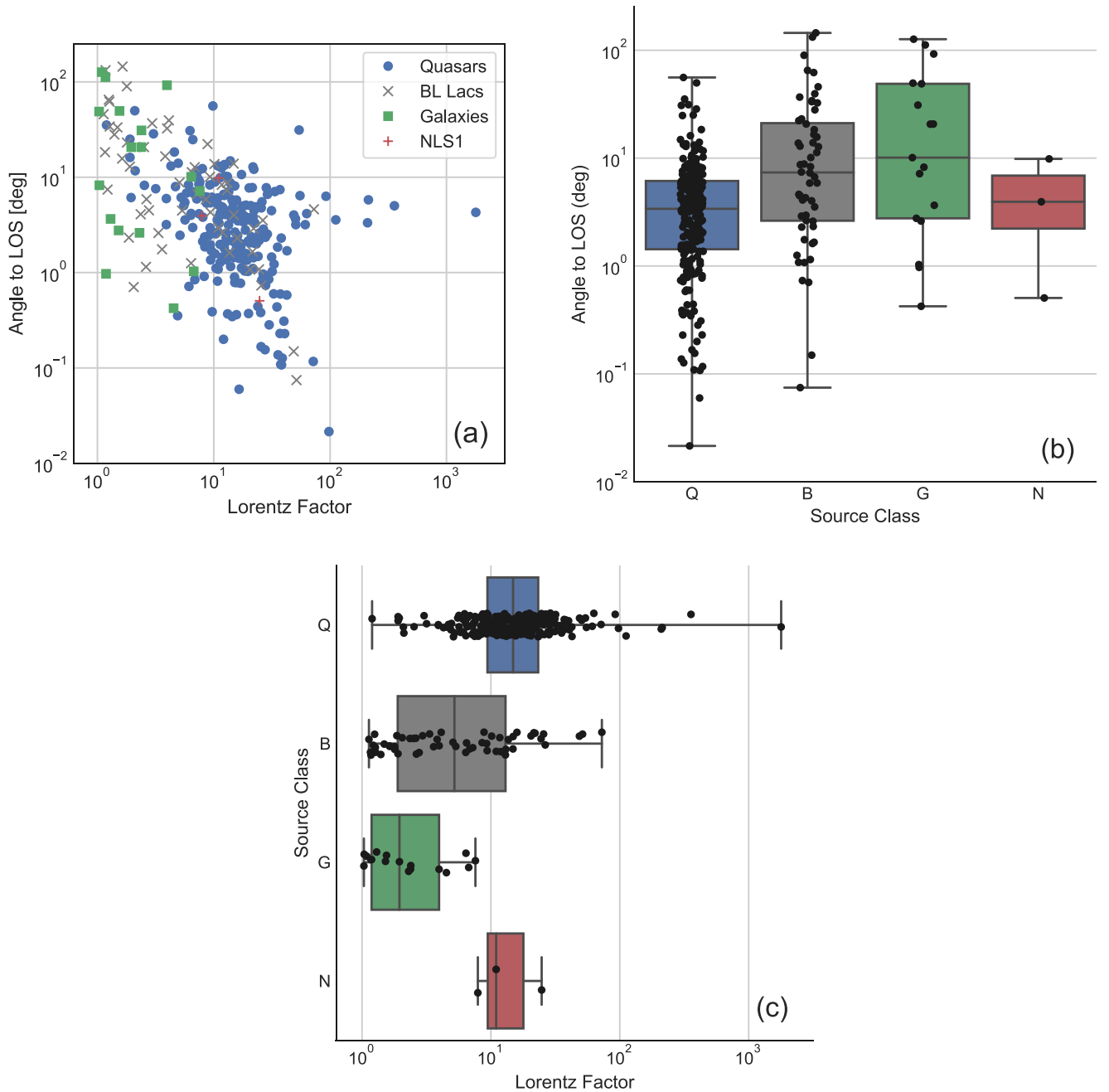


Figure 12. Panel (a) plots angle to the line of sight, θ , against Lorentz Factor, Γ , for all 309 sources with apparent speeds and median brightness temperature measurements. Panels (b) and (c) illustrate the distributions of these quantities as a function of optical class, where “Q” = quasars, “B” = BL Lacs, “G” = radio galaxies, and “N” = narrow-line Seyfert Is. The filled regions of the box plots show in the interquartile range of each optical class, while the whiskers show the full extent of the data. Individual data points are shown as a scatter plot over the box plot to better illustrate the range and density of the data.

There are five sources from our whole 309-jet sample that have estimated Lorentz factors $\Gamma > 100$, and all are quasars with Doppler factors much smaller than their apparent speeds. All five sources have multiple fast motions observed in their jets, so the discrepancy is unlikely to be caused by a single outlier speed. Three of these sources, 0519+011, 0529+075, and 1420+326, have estimated Doppler factors < 1.0 , making them highly improbable to be observed at such large redshifts, and we note that Liodakis et al. (2018) report variability Doppler factors > 15 for each of them. The most extreme case is 0519+011, with a Doppler factor of just 0.2 and multiple features showing approximately the same $25c$ apparent motion, leading to an estimated $\Gamma = 1790$. 0519+011 is at a very large

redshift of $z = 2.941$, and its radio core is very dim relative to the downstream jet emission. The jet cores in these cases may suffer from absorption or opacity or may simply have been in an atypically low state during our observations, either of which could lead to a larger than expected departure from our assumed value for $T_{b,int}$.

There are also five jets that have estimated viewing angles to the line of sight, $\theta > 90^\circ$. Three of the five are galaxies and two are HSP BL Lacs, all at low redshift with $\delta < 1$ and $\beta_{app} < 1$. While a $\theta > 90^\circ$ value is nonphysical for an approaching jet, uncertainties in the Doppler factor consistent with our estimates given above can bring them to more reasonable viewing angles. For example, 1957+405 (Cygnus A), has $\theta = 127^\circ$ from this

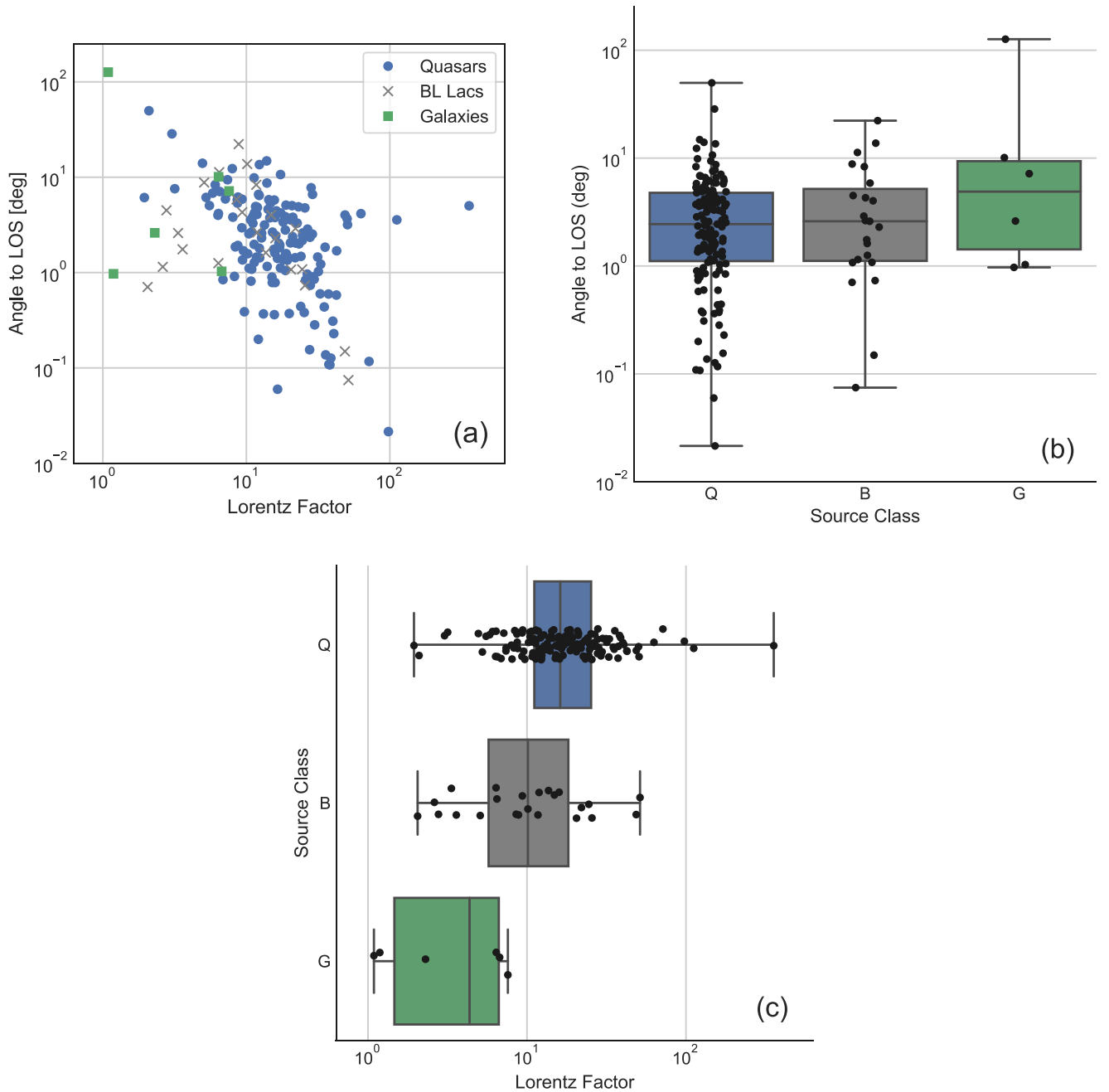


Figure 13. Panel (a) plots angle to the line of sight, θ , against Lorentz Factor, Γ , for the MOJAVE 1.5 Jy QC sample. Panels (b) and (c) illustrate the distributions of these quantities as function of optical class, where “Q” = quasars, “B” = BL Lacs, and “G” = radio galaxies. The filled regions of the box plots show in the interquartile range of each optical class, while the whiskers show the full extent of the data. Individual data points are shown as a scatter plot over the box plot to better illustrate the range and density of the data.

analysis, but if its Doppler factor was $1.5 \times$ higher, it would be at $\theta = 60^\circ$, consistent with the $45^\circ < \theta < 70^\circ$ range estimated by Cohen et al. (2007).

Finally, there may be some jets for which the fastest apparent speed is not a good indicator of the flow speed, and these cases will have poor estimates of Γ and θ . In Section 3.2.2 we examine the impact on our results if we had used the median instead of the fastest speed in our analysis; however, there may be individual sources for which the measured speeds themselves are not reliable tracers of the flow. One possible example is 1228+126 (M87), which has a Doppler factor of $\delta = 1.8$ in our analysis, consistent with the jet-counter-jet ratio

of 10–15 reported by Kovalev et al. (2007); however, its fastest apparent speed is just $0.02c$, as reported in MOJAVEXVIII, giving an angle to the line of sight of $\theta = 1^\circ$ in our analysis. Kovalev et al. (2007) discuss the apparent speed issue for M87 in depth, including the possibility that we are seeing slow pattern motions in a spine-sheath structure. Walker et al. (2018) used high cadence 43 GHz VLBA observations to show that the apparent speed of the jet increases from $\lesssim 0.5c$ to $\gtrsim 2c$ over the first two milli-arcseconds. Combined with our $\delta = 1.8$, these speeds would change the estimated angle to the line of sight for M87 to be in the range 22° – 33° .

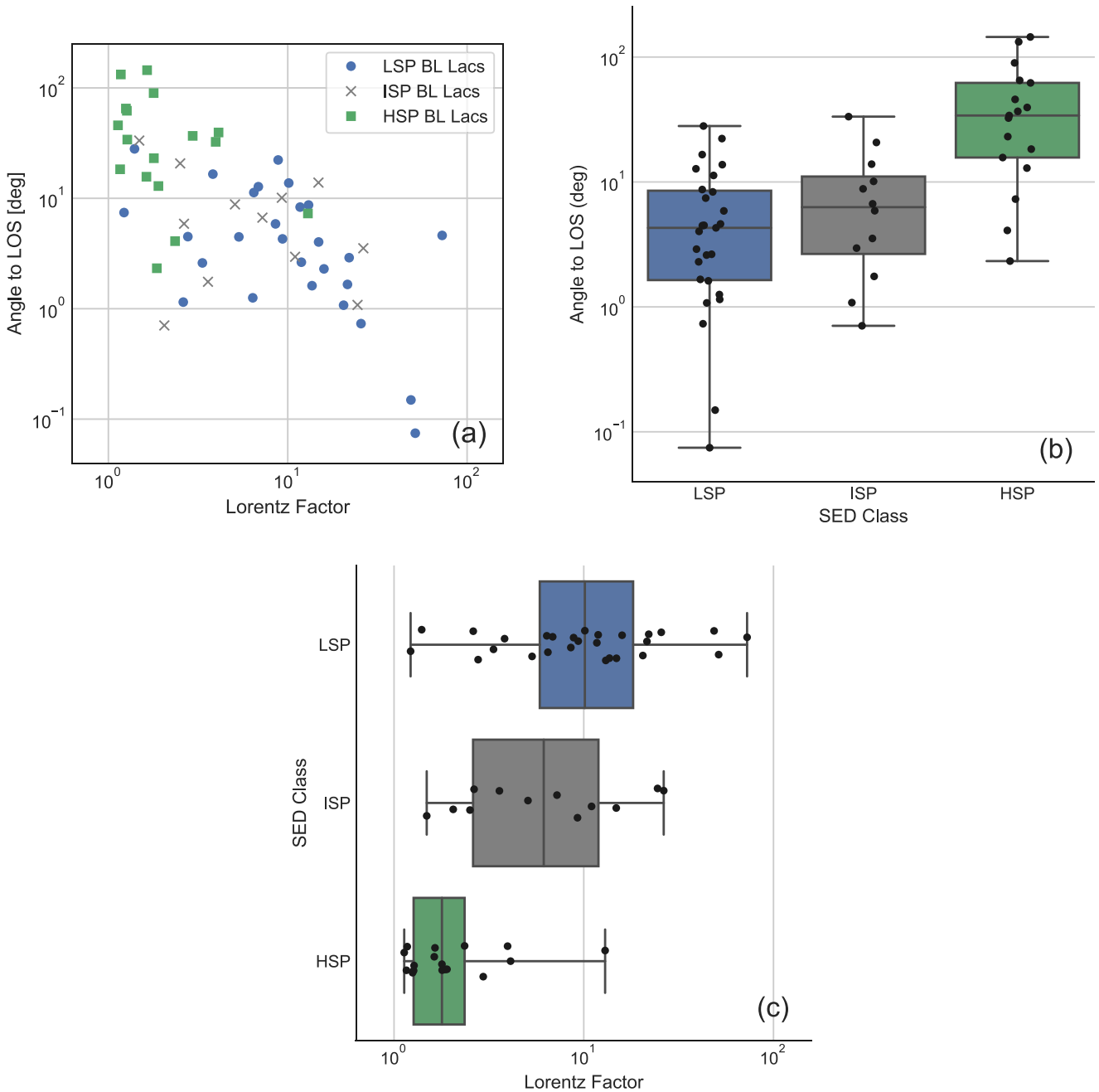


Figure 14. Panel (a) plots angle to the line of sight, θ , against Lorentz Factor, Γ , for all BL Lac objects. Panels (b) and (c) illustrate the distributions of these quantities as function of SED class, where the “LSP,” “ISP,” and “HSP” abbreviations indicate Low, Intermediate, and High Spectral Peak sources respectively. The filled regions of the box plots show in the interquartile range of each SED class, while the whiskers show the full extent of the data. Individual data points are shown as a scatter plot over the box plot to better illustrate the range and density of the data.

3.2.1. Trends with δ , Γ , θ , and θ_{src}

Figures 12, 13, and 14 show scatter plots of viewing angle versus Lorentz factor for our entire heterogeneous sample, the MOJAVE 1.5 Jy QC flux-density-limited sample, and BL Lacs divided by SED class respectively. Each of these scatter plots is accompanied by two sets of box plots, which show the distributions of these quantities as a function of optical or SED class. Note that these figures and the following discussion are complementary to the brightness temperature plots and discussion in Section 3.1.1 as we are taking brightness temperature to be directly proportional to the Doppler factor.

Figure 12 for our whole, heterogeneous sample has 233 quasars, 56 BL Lacs, 17 radio galaxies, and 3 narrow-line Seyfert I galaxies. Quasars have larger Lorentz factors and smaller viewing angles than both BL Lacs and galaxies as confirmed by Anderson–Darling tests that show the probability they are drawn from the same distribution is $p < 0.001$ in each case. If we restrict the comparison to just LSP quasars ($n = 227$) and BL Lacs ($n = 27$), the Lorentz factor difference still holds ($p = 0.010$), but we no longer detect a viewing angle difference ($p = 0.22$), consistent with the findings of Liodakis et al. (2018).

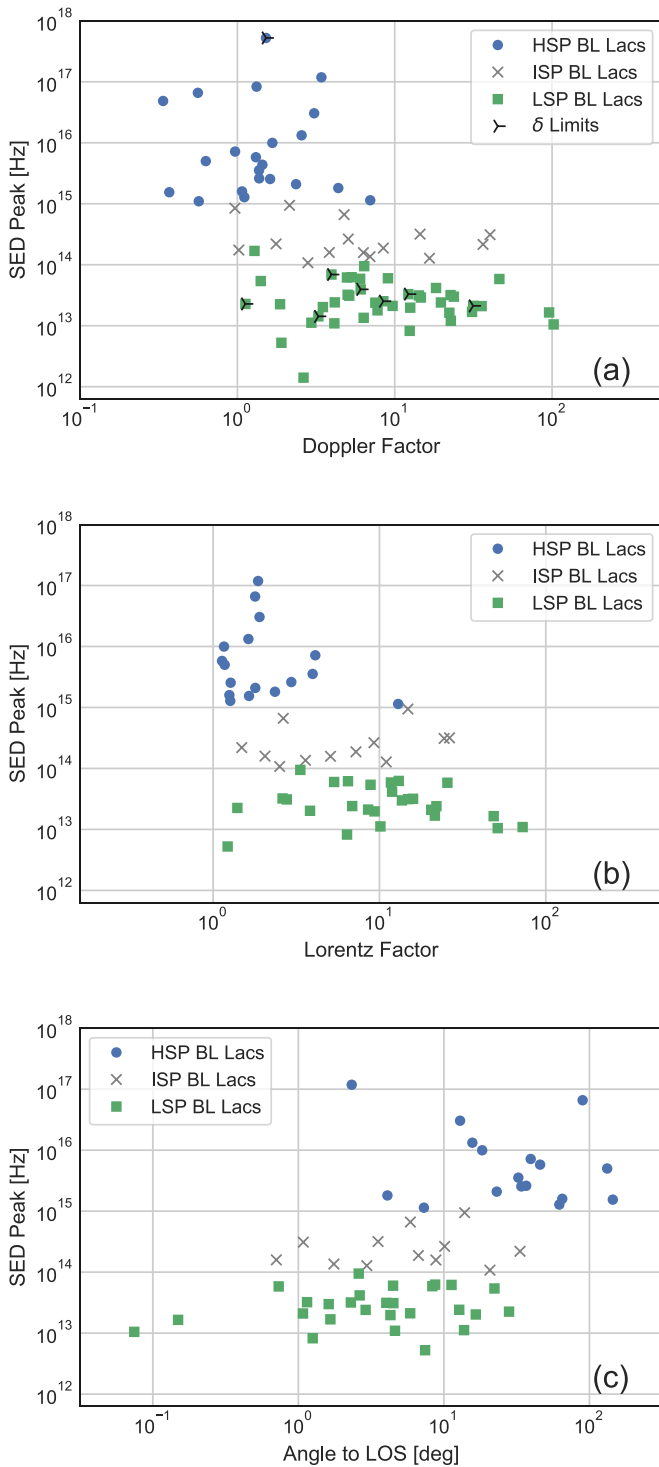


Figure 15. SED peak frequency in the host galaxy frame vs. Doppler factor (panel (a)), Lorentz Factor (panel (b)), and angle to the line of sight (panel (c)) for BL Lacs identified by SED class. Panel (a) includes 79 BL Lacs for which we could estimate the Doppler factor from their median brightness temperature. Panels (b) and (c) include just the 56 BL Lacs for which we could also use their measured apparent speeds to estimate their other properties as described in Section 2.2.3.

The MOJAVE 1.5 Jy QC flux-density-limited sample has 149 quasars, 23 BL Lacs, and just 6 radio galaxies in Figure 13. For Lorentz factor, we find all three distributions differ from one another ($p = 0.004$ for quasars versus BL Lacs, $p < 0.001$ for quasars versus galaxies, $p = 0.011$ for BL Lacs versus

galaxies), with quasars having the largest Lorentz factors and galaxies the smallest in the sequence. For viewing angles, we can detect no difference between the classes with our Anderson–Darling tests, although we note the number of galaxies is quite small ($n = 6$) and includes M87, which may have had its viewing angle underestimated as described in Section 3.2.

We note that the Lorentz factor differences between quasars and radio galaxies described above are driven by our flux-density-limited selection criteria where only nearby radio galaxies have sufficient flux-density without the need for large Doppler beaming factors to make it into our sample.

Finally, we look at BL Lacs as a function of SED class in Figure 14, which has 27 LSP, 12 ISP, and 17 HSP BL Lacs. We cannot detect a difference in either Lorentz factor or viewing angle between LSP and ISP BL Lacs with $p > 0.25$ for both quantities; however, HSP BL Lacs have smaller Lorentz factors and larger viewing angles than both LSPs ($p < 0.001$ for both quantities) and ISPs ($p = 0.002$ for Lorentz factor and $p = 0.001$ for viewing angle). When combined with our finding in Section 3.1.1 that HSP BL Lacs have lower brightness temperatures, and therefore lower Doppler factors, than the other classes, we get the consistent picture in Figure 15, which shows all three quantities as a function of SED peak frequency. HSP BL Lacs appear distinct from ISP and LSP BL Lacs with lower Doppler and Lorentz factors and larger viewing angles. This is consistent with the analysis of Piner & Edwards (2018) who estimate a maximum Lorentz factor of about 4 for this class on the basis of observed motions.

In Section 3.1.1, we investigated a correlation between γ -ray Luminosity and median brightness temperature, most likely due to a common Doppler boosting of the radio cores and the γ -ray emission. Figure 16 examines this question further by plotting γ -ray luminosity against each of the intrinsic quantities estimated by our analysis. The strongest correlation is clearly with the Doppler factor, and the somewhat weaker correlations with Lorentz factor and viewing angle are likely a consequence of their necessary role in producing highly Doppler boosted emission. This is consistent with the finding of Savolainen et al. (2010) that LAT γ -ray detected blazars differ significantly in their Doppler factor distribution from non-LAT detected blazars. We do not see a strong trend with the angle to the line of sight in the comoving emission frame, θ_{src} , in contradiction to the results of Savolainen et al. (2010) from a smaller sample, but consistent with the findings of Liidakis et al. (2018), who do not detect a difference in source-frame viewing angle distribution between LAT detected and non-detected sources.

3.2.2. Fastest versus Median Speeds

In Section 2.2 we examined three possible choices for representing the apparent jet speed in this analysis, and we chose to use the fastest apparent speed as it correlated most strongly with median brightness temperature and was the least likely to be contaminated by slowly moving, “quasistationary,” features in the jets. An additional complicating factor is that jets are still becoming organized on these length scales and show evidence for acceleration and collimation (e.g., Komissarov et al. 2007; Homan et al. 2015; Chatterjee et al. 2019; Kovalev et al. 2020c), and it is possible that choosing the fastest apparent speed may better characterize the jet downstream from the core, rather than the core region itself where the brightness temperature measurements are made. When we looked at the speed of the feature that was closest to the jet core in its first epoch, we found it correlated much more

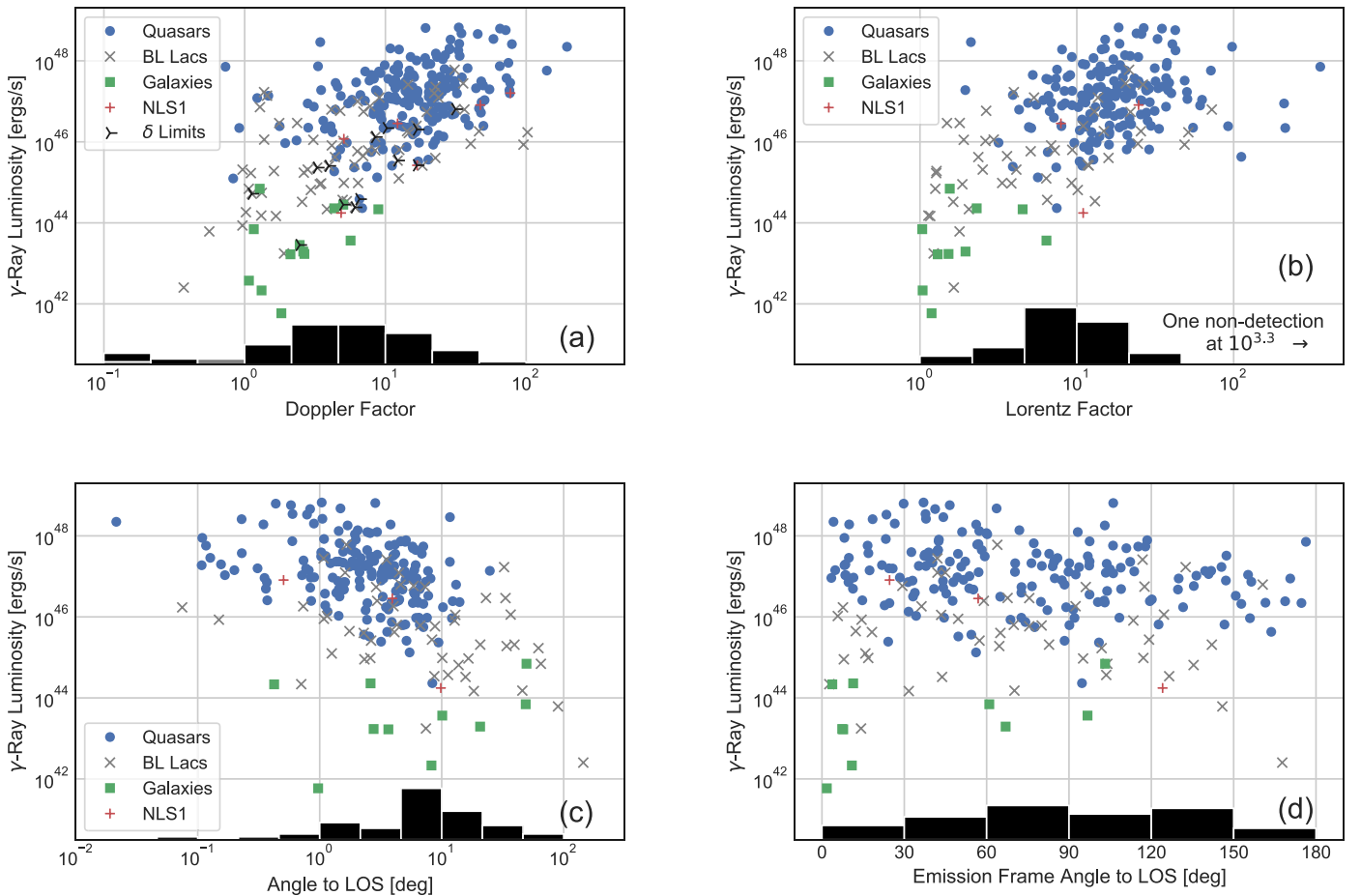


Figure 16. γ -ray luminosity vs. Doppler factor (panel (a)), Lorentz factor (panel (b)), angle to the line of sight (panel (c)), and angle to the line of sight in the comoving emission frame (panel (d)) for Fermi/LAT-detected AGN in our sample. The histogram at the bottom of each panel shows the distribution of sources without Fermi/LAT-detections. Panel (a) includes 351 sources for which we could estimate the Doppler factor from their median brightness temperature, 60 of which do not have a Fermi/LAT detection. Panels (b) through (d) include 285 sources for which we could also use their measured apparent speeds to estimate their other properties as described in Section 2.2.3, 49 of which do not have a Fermi/LAT detection. Only sources with known redshifts and with a galactic latitude $|b| > 10^\circ$ are included in this plot.

poorly with apparent brightness temperature, likely due to contributions from quasistationary shocks near the jet origin (e.g., Lister et al. 2009; Jorstad et al. 2017); however, the median jet speed correlated almost as well with core brightness temperature as the fastest speed and might have made a reasonable alternative for this analysis.

If we had chosen to represent jets by their median apparent speed rather than their fastest apparent speed, very few of our results would change. We would conclude the intrinsic brightness temperature was about 40% larger, $T_{b,int} = 10^{10.762}$ K, and would find correspondingly lower Doppler factors for each source. Those lower Doppler values combined with their median speeds would lead to smaller estimated Lorentz factors and larger estimated viewing angles for most sources by a similar factor. However, despite these changes to δ , Γ , and θ , the relationships between these quantities and optical class, SED class, and γ -ray luminosity all remain the same without any appreciable change to the significant statistical relationships and trends discussed in our analysis above using the fastest speed.

3.3. Intrinsic T_b and Energy Balance in Jet Cores

In Section 2.2 we find the typical intrinsic Gaussian peak brightness temperature for jets in their median state to be $10^{10.609 \pm 0.067} = 4.1(\pm 0.6) \times 10^{10}$ K. However, as discussed in

Section 2.1, we found that the Gaussian peak brightness temperature over-predicted the center brightness temperature of a range of homogeneous sphere models by a factor of 1.8. This factor did not depend on whether the sphere was barely resolved, and represented almost entirely by the Gaussian, or well resolved, with the Gaussian being fitted to the central region and the remainder of the sphere being fitted with CLEAN components. Because this factor is constant, it cancels out and does not impact our analysis of Doppler factors and other derived quantities discussed above; however, to compare to other programs, which typically assume sphere or disk geometries, we take this factor of 1.8 to convert¹⁸ our measured Gaussian brightness temperatures to those used or derived by variability approaches (e.g., Hovatta et al. 2009; Jorstad et al. 2017; Liodakis et al. 2017, 2018). With the application of this factor, the typical intrinsic brightness temperatures of jets in our program in their median state becomes $2.3(\pm 0.3) \times 10^{10}$ K.

Following Readhead (1994), it has been common practice in Doppler factor studies to assume jets are near an equipartition balance between the magnetic field and particle energy in the emission region, even during flares, with a canonical value of $T_{b,int} \simeq 5.0 \times 10^{10}$ K (e.g., Hovatta et al. 2009; Liodakis et al.

¹⁸ A factor of 1.8 was also estimated by Tingay et al. (2001) by comparing the (u, v) -plane profile of a Gaussian to an optically thick sphere.

2017); however, as noted in Section 2.2.4, Liodakis et al. (2018) found a much larger value of $T_{b,int} = 2.8 \times 10^{11}$ K, approaching the $\approx 10^{11.5}$ K inverse Compton limit (Kellermann & Pauliny-Toth 1969; Readhead 1994) and perhaps consistent with the diamagnetic limit suggested by Singal (1986). In this paper, we have characterized the intrinsic brightness temperatures of jets, not in their flaring state but rather in their median state, and we find jets to be at or below equipartition in that median state, suggesting that jet cores may even be magnetic field dominated in their lower brightness states. We note that Lee (2013) reported even lower intrinsic brightness temperatures at 86 GHz for compact radio jets, suggesting magnetic field dominance closer to the central engine, although Lee et al. (2016) also concluded that the change in brightness temperature with frequency in VLBI jets cores indicates acceleration along the jet.

As discussed in Section 3.1, observed brightness temperatures within individual jets can span up to an order of magnitude or more in the most variable jets. The typical ratio between the maximum observed brightness temperature and its median value for the same jet is a factor of a few, and even if these variations are entirely due to changes in the intrinsic brightness temperature, we would still find intrinsic brightness temperatures for most sources in their flaring states below the inverse Compton limit of $10^{11.5}$ K (Kellermann & Pauliny-Toth 1969; Readhead 1994) or even the typical flaring state value of 2.8×10^{11} K deduced by Liodakis et al. (2018). This difference between the maximum brightness temperatures we observe for most sources and the typical flaring value found by Liodakis et al. (2018) may simply be due to the fact that we are measuring the brightness temperature of the core region of the jet as a whole, and even during an outburst, the core region may not consist of just a single flaring component. Indeed, this suggestion is supported by the *RadioAstron* space VLBI measurements, which can detect smaller subcomponents in the jet core (Kovalev et al. 2020b). They indicate higher peak brightness temperatures at 22 GHz in at least two powerful AGN jets at similar epochs to those we observed from the VLBA alone at 15 GHz. For example in 3C 273, *RadioAstron* at 22 GHz measured an observed brightness temperature of 1.4×10^{13} K in 2013 February, an order of magnitude larger than our 1.12×10^{12} K measurement made eight days later (Kovalev et al. 2016), and in BL Lac, *RadioAstron* measured a 22 GHz brightness temperature of $> 2 \times 10^{13}$ K a little more than a month before our measurement of 2.11×10^{12} K (Gómez et al. 2016). Note that both of these jets have estimated Doppler factors $\delta \approx 20$ in our analysis, so the intrinsic brightness temperatures implied by the *RadioAstron* results are a couple of times larger than the flaring state value given by Liodakis et al. (2018),¹⁹ confirming that compact regions in the jet can be strongly particle dominated and approach the inverse Compton limit.

4. Summary and Conclusions

We have made multiepoch, parsec-scale core brightness temperature measurements of 447 AGN jets from the MOJAVE VLBA program; 206 of these AGN are members of the MOJAVE 1.5 Jy QC flux-density-limited sample. We characterized each jet by its median core brightness temperature and variability over time and examined trends with optical class, SED class, and γ -ray

luminosity computed from the Fermi/LAT 10 yr point-source catalog (Ajello et al. 2020).

Combined with our recently updated apparent speed measurements reported in MOJAVEXVIII, we followed the approach of Homan et al. (2006) to estimate the typical intrinsic Gaussian brightness temperature of a jet core in its median state, $T_{b,int} = 10^{10.609 \pm 0.067} = 4.1 (\pm 0.6) \times 10^{10}$ K. We used this value to derive estimates for the Doppler factor from the observed median brightness temperature for 447 sources in our sample, $\delta = T_{b,obs}/T_{b,int}$, and compared our results to those from other programs. For the 309 AGN jets with both apparent speed and brightness temperature data, we also estimated their intrinsic Lorentz factors and viewing angles to the line of sight.

Our main results are as follows:

1. We measured the parsec-scale core brightness temperature of each AGN jet in every epoch by fitting a single Gaussian to the core region alone and modeling the remainder of the jet by CLEAN components. We find that the observed Gaussian brightness temperature of the jet core of a given source varies over time by a factor of a few up to about an order of magnitude, with a few extreme cases having larger variations; however, the differences between AGN jets in our sample can be much larger, with median values spanning two and a half to three orders of magnitude. The range of observed median brightness temperatures across our sample is consistent with Doppler boosting being the primary difference between AGN jets in their median state.

2. Median core brightness temperatures differ between AGN based on their optical classes and synchrotron peak classifications. Quasars and BL Lacs have larger observed brightness temperatures, and therefore Doppler beaming factors, than radio galaxies, as one would expect according to unified models (e.g., Urry & Padovani 1995), whether we consider just the MOJAVE 1.5 Jy QC flux-density-limited sample or our entire heterogeneous sample. If we consider only LSP quasars and BL Lacs, we do not detect a difference between them in terms of their median core brightness temperatures, indicating they have similar levels of Doppler beaming. However, within the BL Lac class itself, HSP BL Lacs have distinctly lower median brightness temperatures than their intermediate and LSP counterparts, indicating they are less beamed than those whose SEDs peak at lower frequencies, consistent with earlier findings (e.g., Niappola et al. 2008; Lister et al. 2011; Piner & Edwards 2018).

3. Combined with apparent speed measurements, the Doppler factor estimates from the observed median brightness temperatures allowed us to measure and compare the Lorentz factors and viewing angles of 309 of our AGN jets, 178 of which were members of the MOJAVE 1.5 Jy QC sample. The Lorentz factor distributions of quasars, BL Lacs, and radio galaxies all differ from one another with quasars having the largest Lorentz factors and radio galaxies the smallest. If we consider just LSP quasars and BL Lacs, we still detect a significant Lorentz factor difference between them but do not detect a difference in viewing angle distribution, similar to the findings of Liodakis et al. (2018). HSP BL Lacs appear distinct from ISP and LSP BL Lacs with lower Lorentz factors and larger viewing angles to the line of sight.

4. Median core brightness temperatures, and by extension jet Doppler factors, correlate strongly with γ -ray luminosity for LAT detected jets, and we confirm earlier findings that LAT detected jets have larger core brightness temperatures than nondetected jets (e.g., Kovalev et al. 2009; Lister et al. 2011).

¹⁹ This comparison includes the factor of 1.8 difference between sphere/disk model used in the variability analysis and the Gaussian brightness temperatures used by *RadioAstron*.

We also see clear trends between γ -ray luminosity and Lorentz factor and viewing angle to the line of sight; however, the strongest relationship appears to be with median core brightness temperature/Doppler factor, and the trends with Lorentz factor and viewing angle are likely a consequence of their necessary role in producing highly Doppler boosted emission. We do not see a strong trend with angle to the line of sight in the comoving emission frame.

5. We found the typical intrinsic Gaussian peak brightness temperature for jets cores in their median state to be $4.1(\pm 0.6) \times 10^{10}$ K. Our Gaussian brightness temperatures are a factor of 1.8 times larger than the spherical/disk geometries used in variability Doppler factor analyses. The best geometry to represent the core region is unknown; however, regardless of whether or not we apply this geometrical factor, we find the jet cores to be at or below the typically assumed value for equipartition between magnetic field and particle energies of 5.0×10^{10} K (e.g., Readhead 1994; Lähtenmäki & Valtaoja 1999) in their median state.

We thank Margo Aller, Alexander Plavin, and the other members of the MOJAVE team for helpful conversations and their other contributions that made this work possible. The MOJAVE project was supported by NASA-Fermi grants 80NSSC19K1579, NNX15AU76G and NNX12A087G. D.C. H. was supported by NSF grant AST-0707693. Y.Y.K. and A. B.P. were supported by the Russian Science Foundation grant 21-12-00241. A.V.P. was supported by the Russian Foundation for Basic Research grant 19-32-90140. T.H. was supported by the Academy of Finland projects 317383, 320085, and 322535. T.S. was partly supported by the Academy of Finland projects 274477 and 315721. The National Radio Astronomy Observatory is a facility of the National Science Foundation operated under cooperative agreement by Associated Universities, Inc. This work made use of the Swinburne University of Technology software correlator (Deller et al. 2011), developed as part of the Australian Major National Research Facilities Program and operated under licence. This research has made use of data from the OVRO 40 m monitoring program Richards et al. (2011), which is supported in part by NASA grants NNX08AW31G, NNX11A043G, and NNX14AQ89G and NSF grants AST-0808050 and AST-1109911. This research has made use of NASA's Astrophysics Data System. This research has made use of the NASA/IPAC Extragalactic Database (NED), which is operated by the Jet Propulsion Laboratory, California Institute of Technology, under contract with the National Aeronautics and Space Administration.

Facilities: VLBA, OVRO:40 m, NED, ADS.

ORCID iDs

D. C. Homan  <https://orcid.org/0000-0002-4431-0890>
M. H. Cohen  <https://orcid.org/0000-0002-8033-5972>
T. Hovatta  <https://orcid.org/0000-0002-2024-8199>
K. I. Kellermann  <https://orcid.org/0000-0002-0093-4917>
Y. Y. Kovalev  <https://orcid.org/0000-0001-9303-3263>
M. L. Lister  <https://orcid.org/0000-0003-1315-3412>
A. V. Popkov  <https://orcid.org/0000-0002-0739-700X>
A. B. Pushkarev  <https://orcid.org/0000-0002-9702-2307>
E. Ros  <https://orcid.org/0000-0001-9503-4892>
T. Savolainen  <https://orcid.org/0000-0001-6214-1085>

References

- Aartsen, M. G., Ackermann, M., Adams, J., et al. 2020, *PhRvL*, **124**, 051103
Abdo, A. A., Ackermann, M., Ajello, M., et al. 2009a, *ApJL*, **707**, L142
Abdo, A. A., Ackermann, M., Ajello, M., et al. 2009b, *ApJ*, **707**, 55
Abdo, A. A., Ackermann, M., Ajello, M., et al. 2010, *ApJ*, **715**, 429
Abolfathi, B., Aguado, D. S., Aguilar, G., et al. 2018, *ApJS*, **235**, 42
Abramowski, A., Aharonian, F., Ait Benkhali, F., et al. 2015, *ApJ*, **802**, 65
Ackermann, M., Ajello, M., Allafort, A., et al. 2011, *ApJ*, **743**, 171
Ackermann, M., Ajello, M., Atwood, W. B., et al. 2015, *ApJ*, **810**, 14
Adelman-McCarthy, J. K., Agüeros, M. A., Allam, S. S., et al. 2006, *ApJS*, **162**, 38
Adelman-McCarthy, J. K., Agüeros, M. A., Allam, S. S., et al. 2008, *ApJS*, **175**, 297
Afanas'Ev, V. L., Dodonov, S. N., Moiseev, A. V., et al. 2006, *ARep*, **50**, 255
Agudo, I., Bach, U., Krichbaum, T. P., et al. 2007, *A&A*, **476**, L17
Aihara, H., Allende Prieto, C., An, D., et al. 2011, *ApJS*, **193**, 29
Ajello, M., Angioni, R., Axelsson, M., et al. 2020, *ApJ*, **892**, 105
Ajello, M., Atwood, W. B., Baldini, L., et al. 2017, *ApJS*, **232**, 18
Albert, J., Aliu, E., Anderhub, H., et al. 2007, *ApJL*, **667**, L21
Aldcroft, T. L., Bechtold, J., & Elvis, M. 1994, *ApJS*, **93**, 1
Aller, M. F., Aller, H. D., & Hughes, P. A. 1992, *ApJ*, **399**, 16
Álvarez Crespo, N., Massaro, F., Milisavljevic, D., et al. 2016, *AJ*, **151**, 95
Antonucci, R. R. J., Hickson, P., Miller, J. S., & Olszewski, E. W. 1987, *AJ*, **93**, 785
Bade, N., Fink, H. H., Engels, D., et al. 1995, *A&AS*, **110**, 469
Baker, J. C., Hunstead, R. W., Kapahi, V. K., & Subrahmanya, C. R. 1999, *ApJS*, **122**, 29
Becerra González, J., Acosta-Pulido, J. A., Boschin, W., et al. 2021, *MNRAS*, **504**, 5258
Best, P. N., Peacock, J. A., Brookes, M. H., et al. 2003, *MNRAS*, **346**, 1021
Boisse, P., & Bergeron, J. 1988, *A&A*, **192**, 1
Boksenberg, A., Briggs, S. A., Carswell, R. F., Schmidt, M., & Walsh, D. 1976, *MNRAS*, **177**, 43P
Browne, I. W. A., Savage, A., & Bolton, J. G. 1975, *MNRAS*, **173**, 87P
Burbidge, E. M. 1970, *ApJL*, **160**, L33
Carangelo, N., Falomo, R., Kotilainen, J., Treves, A., & Ulrich, M.-H. 2003, *A&A*, **412**, 651
Chang, Y.-L., Arsioli, B., Giommi, P., & Padovani, P. 2017, *A&A*, **598**, A17
Chang, Y. L., Arsioli, B., Giommi, P., Padovani, P., & Brandt, C. H. 2019, *A&A*, **632**, A77
Chatterjee, K., Liska, M., Tchekhovskoy, A., & Markoff, S. B. 2019, *MNRAS*, **490**, 2200
Chavushyan, V. 2013, private communication
Chavushyan, V., Mujica, R., Gorshkov, A. G., et al. 2001, *ARep*, **45**, 79
Chiaro, G., Salvetti, D., La Mura, G., et al. 2016, *MNRAS*, **462**, 3180
Cohen, M. H., Cannon, W., Purcell, G. H., et al. 1971, *ApJ*, **170**, 207
Cohen, M. H., Lister, M. L., Homan, D. C., et al. 2007, *ApJ*, **658**, 232
Cohen, R. D., Smith, H. E., Junkkarinen, V. T., & Burbidge, E. M. 1987, *ApJ*, **318**, 577
Davidson-Pilon, C., Kalderstam, J., Jacobson, N., et al. 2020, *CamDavidsonPilon/lifelines*: v0.24.15, Zenodo, doi:10.5281/zenodo.3934629
de Grijp, M. H. K., Keel, W. C., Miley, G. K., Goudfrooij, P., & Lub, J. 1992, *A&AS*, **96**, 389
Deller, A. T., Brisken, W. F., Phillips, C. J., et al. 2011, *PASP*, **123**, 275
Denicoló, G., Terlevich, R., Terlevich, E., et al. 2005, *MNRAS*, **356**, 1440
di Serego-Alighieri, S., Danziger, I. J., Morganti, R., & Tadhunter, C. N. 1994, *MNRAS*, **269**, 998
Drinkwater, M. J., Webster, R. L., Francis, P. J., et al. 1997, *MNRAS*, **284**, 85
Eckart, A., Witzel, A., Biermann, P., et al. 1986, *A&A*, **168**, 17
Ellison, S. L., Yan, L., Hook, I. M., et al. 2001, *A&A*, **379**, 393
Eracleous, M., & Halpern, J. P. 1994, *ApJS*, **90**, 1
Eracleous, M., & Halpern, J. P. 2004, *ApJS*, **150**, 181
Falco, E. E., Kochanek, C. S., & Muñoz, J. A. 1998, *ApJ*, **494**, 47
Falco, E. E., Kurtz, M. J., Geller, M. J., et al. 1999, *PASP*, **111**, 438
Falomo, R., Scarpa, R., & Bersanelli, M. 1994, *ApJS*, **93**, 125
Fricke, K. J., Kollatschny, W., & Witzel, A. 1983, *A&A*, **117**, 60
Gelderman, R., & Whittle, M. 1994, *ApJS*, **91**, 491
Glikman, E., Helfand, D. J., White, R. L., et al. 2007, *ApJ*, **667**, 673
Goldoni, P., Pita, S., Boisson, C., et al. 2021, *A&A*, **650**, 106
Gómez, J. L., Lobanov, A. P., Bruni, G., et al. 2016, *ApJ*, **817**, 96
Greisen, E. W. 2003, in *AIPS, the VLA, and the VLBA*, ed. A. Heck (Dordrecht: Springer), 109
Guijosa, A., & Daly, R. A. 1996, *ApJ*, **461**, 600
Halpern, J. P., & Eracleous, M. 1997, *IAUC*, **6639**, 2

- Halpern, J. P., Eracleous, M., & Mattox, J. R. 2003, *AJ*, 125, 572
- Healey, S. E., Romani, R. W., Cotter, G., et al. 2008, *ApJS*, 175, 97
- Heidt, J., Nilsson, K., Fried, J. W., Takalo, L. O., & Sillanpää, A. 1999, *A&A*, 348, 113
- Heidt, J., Tröller, M., Nilsson, K., et al. 2004, *A&A*, 418, 813
- Henstock, D. R., Browne, I. W. A., Wilkinson, P. N., & McMahon, R. G. 1997, *MNRAS*, 290, 380
- Hervet, O., Boisson, C., & Sol, H. 2015, *A&A*, 578, A69
- Ho, L. C., & Kim, M. 2009, *ApJS*, 184, 398
- Homan, D. C., Kovalev, Y. Y., Lister, M. L., et al. 2006, *ApJL*, 642, L115
- Homan, D. C., Lister, M. L., Kovalev, Y. Y., et al. 2015, *ApJ*, 798, 134
- Hook, I. M., McMahon, R. G., Irwin, M. J., & Hazard, C. 1996, *MNRAS*, 282, 1274
- Hovatta, T., Lindfors, E., Kiehlmann, S., et al. 2021, *A&A*, 650, A83
- Hovatta, T., Valtaoja, E., Tornikoski, M., & Lähteenmäki, A. 2009, *A&A*, 494, 527
- Huchra, J. P., Macri, L. M., Masters, K. L., et al. 2012, *ApJS*, 199, 26
- Huchra, J. P., Vogeley, M. S., & Geller, M. J. 1999, *ApJS*, 121, 287
- Hughes, P. A., Aller, H. D., & Aller, M. F. 1989, *ApJ*, 341, 54
- Hunstead, R. W., Murdoch, H. S., & Shobbrook, R. R. 1978, *MNRAS*, 185, 149
- Hunter, S. D., Bertsch, D. L., Dingus, B. L., et al. 1993, *ApJ*, 409, 134
- IceCube Collaboration, Aartsen, M. G., Ackermann, M., et al. 2018, *Sci*, 361, eaat1378
- Jackson, N., & Browne, I. W. A. 1991, *MNRAS*, 250, 414
- Jauncey, D. L., Batty, M. J., Wright, A. E., Peterson, B. A., & Savage, A. 1984, *ApJ*, 286, 498
- Jones, D. H., Read, M. A., Saunders, W., et al. 2009, *MNRAS*, 399, 683
- Jones, D. H., Saunders, W., Read, M., & Colless, M. 2005, *PASA*, 22, 277
- Jorstad, S. G., Marscher, A. P., Lister, M. L., et al. 2005, *AJ*, 130, 1418
- Jorstad, S. G., Marscher, A. P., Morozova, D. A., et al. 2017, *ApJ*, 846, 98
- Junkkarinen, V. 1984, *PASP*, 96, 539
- Kadler, M., Ros, E., Lobanov, A. P., Falcke, H., & Zensus, J. A. 2004, *A&A*, 426, 481
- Kellermann, K. I., & Pauliny-Toth, I. I. K. 1969, *ApJL*, 155, L71
- Klindt, L., van Soelen, B., Meintjes, P. J., & Väisänen, P. 2017, *MNRAS*, 467, 2537
- Komatsu, E., Dunkley, J., Nolta, M. R., et al. 2009, *ApJS*, 180, 330
- Komissarov, S. S., Barkov, M. V., Vlahakis, N., & Königl, A. 2007, *MNRAS*, 380, 51
- Kormendy, J., & Ho, L. C. 2013, *ARA&A*, 51, 511
- Kovalev, Y. A., Kardashev, N. S., Kovalev, Y. Y., et al. 2020a, *AdSpR*, 65, 745
- Kovalev, Y. Y., Aller, H. D., Aller, M. F., et al. 2009, *ApJL*, 696, L17
- Kovalev, Y. Y., Kardashev, N. S., Kellermann, K. I., et al. 2016, *ApJL*, 820, L9
- Kovalev, Y. Y., Kardashev, N. S., Sokolovsky, K. V., et al. 2020b, *AdSpR*, 65, 705
- Kovalev, Y. Y., Kellermann, K. I., Lister, M. L., et al. 2005, *AJ*, 130, 2473
- Kovalev, Y. Y., Lister, M. L., Homan, D. C., & Kellermann, K. I. 2007, *ApJL*, 668, L27
- Kovalev, Y. Y., Pushkarev, A. B., Nokhrina, E. E., et al. 2020c, *MNRAS*, 495, 3576
- Labiano, A., Barthel, P. D., O’Dea, C. P., et al. 2007, *A&A*, 463, 97
- Lähteenmäki, A., & Valtaoja, E. 1999, *ApJ*, 521, 493
- LAMOST DR4 2018, <http://dr4.lamost.org/>
- LAMOST DR6 V2 2019, <http://dr6.lamost.org/>
- Landoni, M., Falomo, R., Treves, A., et al. 2012, *A&A*, 543, A116
- Laurent-Muehleisen, S. A., Kollgaard, R. I., Feigelson, E. D., Brinkmann, W., & Siebert, J. 1999, *ApJ*, 525, 127
- Lawrence, C. R., Pearson, T. J., Readhead, A. C. S., & Unwin, S. C. 1986, *AJ*, 91, 494
- Lawrence, C. R., Zucker, J. R., Readhead, A. C. S., et al. 1996, *ApJS*, 107, 541
- Lee, S.-S. 2013, *JKAS*, 46, 243
- Lee, S.-S., Lobanov, A. P., Krichbaum, T. P., & Zensus, J. A. 2016, *ApJ*, 826, 135
- Liodakis, I., Hovatta, T., Huppenkothen, D., et al. 2018, *ApJ*, 866, 137
- Liodakis, I., Marchili, N., Angelakis, E., et al. 2017, *MNRAS*, 466, 4625
- Lister, M. L., Aller, M., Aller, H., et al. 2011, *ApJ*, 742, 27
- Lister, M. L., Aller, M. F., Aller, H. D., et al. 2018, *ApJS*, 234, 12
- Lister, M. L., Cohen, M. H., Homan, D. C., et al. 2009, *AJ*, 138, 1874
- Lister, M. L., & Homan, D. C. 2005, *AJ*, 130, 1389
- Lister, M. L., Homan, D. C., Hovatta, T., et al. 2019, *ApJ*, 874, 43
- Lister, M. L., Homan, D. C., Kellermann, K. I., et al. 2021, *ApJ*, in press (arXiv:2108.13358)
- Lister, M. L., & Marscher, A. P. 1997, *ApJ*, 476, 572
- Lynds, C. R. 1967, *ApJ*, 147, 837
- Marcha, M. J. M., Browne, I. W. A., Impey, C. D., & Smith, P. S. 1996, *MNRAS*, 281, 425
- Marchã, M. J. M., & Caccianiga, A. 2013, *MNRAS*, 430, 2464
- Marchesini, E. J., Peña-Herazo, H. A., Álvarez Crespo, N., et al. 2019, *Ap&SS*, 364, 5
- Marscher, A. P., & Gear, W. K. 1985, *ApJ*, 298, 114
- Marziani, P., Sulentic, J. W., Dultzin-Hacyan, D., Calvani, M., & Moles, M. 1996, *ApJS*, 104, 37
- Marziani, P., Sulentic, J. W., Zamanov, R., et al. 2003, *ApJS*, 145, 199
- Marzke, R. O., Huchra, J. P., & Geller, M. J. 1996, *AJ*, 112, 1803
- Maslennikov, K. L., Boldycheva, A. V., Malkin, Z. M., & Titov, O. A. 2010, *Ap*, 53, 147
- McConnell, N. J., & Ma, C.-P. 2013, *ApJ*, 764, 184
- McIntosh, D. H., Rieke, M. J., Rix, H.-W., Foltz, C. B., & Weymann, R. J. 1999, *ApJ*, 514, 40
- Meisner, A. M., & Romani, R. W. 2010, *ApJ*, 712, 14
- Meyer, E. T., Fossati, G., Georganopoulos, M., & Lister, M. L. 2011, *ApJ*, 740, 98
- Michel, A., & Huchra, J. 1988, *PASP*, 100, 1423
- Nass, P., Bade, N., Kollgaard, R. I., et al. 1996, *A&A*, 309, 419
- Nieppola, E., Tornikoski, M., & Valtaoja, E. 2006, *A&A*, 445, 441
- Nieppola, E., Valtaoja, E., Tornikoski, M., Hovatta, T., & Kotiranta, M. 2008, *A&A*, 488, 867
- Nilsson, K., Pursimo, T., Villforth, C., et al. 2012, *A&A*, 547, A1
- Oke, J. B. 1978, *ApJL*, 219, L97
- Osmer, P. S., Porter, A. C., & Green, R. F. 1994, *ApJ*, 436, 678
- Owen, F. N., Ledlow, M. J., & Keel, W. C. 1995, *AJ*, 109, 14
- Owen, F. N., Ledlow, M. J., Morrison, G. E., & Hill, J. M. 1997, *ApJL*, 488, L15
- Paiano, S., Falomo, R., Treves, A., & Scarpa, R. 2018, *ApJL*, 854, L32
- Paiano, S., Falomo, R., Treves, A., & Scarpa, R. 2020, *MNRAS*, 497, 94
- Paiano, S., Landoni, M., Falomo, R., Treves, A., & Scarpa, R. 2017a, *ApJ*, 844, 120
- Paiano, S., Landoni, M., Falomo, R., et al. 2017b, *ApJ*, 837, 144
- Pâris, I., Petitjean, P., Aubourg, É., et al. 2018, *A&A*, 613, A51
- Pâris, I., Petitjean, P., Ross, N. P., et al. 2017, *A&A*, 597, A79
- Peña-Herazo, H. A., Amaya-Almazán, R. A., Massaro, F., et al. 2020, *A&A*, 643, A103
- Perlman, E. S., Padovani, P., Giommi, P., et al. 1998, *AJ*, 115, 1253
- Perlman, E. S., Stocke, J. T., Schachter, J. F., et al. 1996, *ApJS*, 104, 251
- Peterson, B. A., Wright, A. E., Jauncey, D. L., & Condon, J. J. 1979, *ApJ*, 232, 400
- Pietsch, W., Bischoff, K., Boller, T., et al. 1998, *A&A*, 333, 48
- Piner, B. G., & Edwards, P. G. 2018, *ApJ*, 853, 68
- Pita, S., Goldoni, P., Boisson, C., et al. 2014, *A&A*, 565, A12
- Plavin, A., Kovalev, Y. Y., Kovalev, Y. A., & Troitsky, S. 2020, *ApJ*, 894, 101
- Plavin, A. V., Kovalev, Y. Y., Kovalev, Y. A., & Troitsky, S. V. 2021, *ApJ*, 908, 157
- Plotkin, R. M., Anderson, S. F., Brandt, W. N., et al. 2010, *AJ*, 139, 390
- Pravdo, S. H., & Marshall, F. E. 1984, *ApJ*, 281, 570
- Punsly, B. 1999, *ApJ*, 516, 141
- Pursimo, T., Ojha, R., Jauncey, D. L., et al. 2013, *ApJ*, 767, 14
- Rau, A., Schady, P., Greiner, J., et al. 2012, *A&A*, 538, A26
- Readhead, A. C. S. 1994, *ApJ*, 426, 51
- Rector, T. A., & Stocke, J. T. 2001, *AJ*, 122, 565
- Ricci, F., Massaro, F., Landoni, M., et al. 2015, *AJ*, 149, 160
- Richards, G. T., Myers, A. D., Gray, A. G., et al. 2009, *ApJS*, 180, 67
- Richards, J. L., Max-Moerbeck, W., Pavlidou, V., et al. 2011, *ApJS*, 194, 29
- Sargent, W. L. W. 1970, *ApJ*, 160, 405
- Savage, A., Browne, I. W. A., & Bolton, J. G. 1976, *MNRAS*, 177, 77P
- Savolainen, T., Homan, D. C., Hovatta, T., et al. 2010, *A&A*, 512, A24
- Sbarufatti, B., Ciprini, S., Kotilainen, J., et al. 2009, *AJ*, 137, 337
- Sbarufatti, B., Treves, A., Falomo, R., et al. 2005, *AJ*, 129, 559
- Sbarufatti, B., Treves, A., Falomo, R., et al. 2006, *AJ*, 132, 1
- Schachter, J. F., Stocke, J. T., Perlman, E., et al. 1993, *ApJ*, 412, 541
- Schmidt, M. 1977, *ApJ*, 217, 358
- Schneider, D. P., Richards, G. T., Hall, P. B., et al. 2010, *AJ*, 139, 2360
- Schneider, D. P., Schmidt, M., & Gunn, J. E. 1999, *AJ*, 117, 40
- Schramm, K.-J., Borgeest, U., Kuehl, D., et al. 1994, *A&AS*, 106, 349
- SDSS Data Release 13 2016, <http://www.sdss.org/dr13/>
- Searle, L., & Bolton, J. G. 1968, *ApJL*, 154, L101
- Shaw, M. S., Filippenko, A. V., Romani, R. W., Cenko, S. B., & Li, W. 2013a, *AJ*, 146, 127
- Shaw, M. S., Romani, R. W., Cotter, G., et al. 2012, *ApJ*, 748, 49
- Shaw, M. S., Romani, R. W., Cotter, G., et al. 2013b, *ApJ*, 764, 135

- Shaw, M. S., Romani, R. W., Healey, S. E., et al. 2009, *ApJ*, **704**, 477
- Shepherd, M. 2011, Difmap: Synthesis Imaging of Visibility Data, Astrophysics Source Code Library, ascl:1103.001
- Shepherd, M. C. 1997, in ASP Conf. Ser. 125, *Astronomical Data Analysis Software and Systems VI*, ed. G. Hunt & H. Payne (San Francisco, CA: ASP), 77
- Singal, A. K. 1986, *A&A*, **155**, 242
- Small, T. A., Sargent, W. L. W., & Steidel, C. C. 1997, *AJ*, **114**, 2254
- Smith, H. E., Burbidge, E. M., Baldwin, J. A., et al. 1977, *ApJ*, **215**, 427
- Sowards-Emmerd, D., Romani, R. W., & Michelson, P. F. 2003, *ApJ*, **590**, 109
- Sowards-Emmerd, D., Romani, R. W., Michelson, P. F., Healey, S. E., & Nolan, P. L. 2005, *ApJ*, **626**, 95
- Spinrad, H., Marr, J., Aguilar, L., & Djorgovski, S. 1985, *PASP*, **97**, 932
- Stadnik, M., & Romani, R. W. 2014, *ApJ*, **784**, 151
- Steidel, C. C., & Sargent, W. L. W. 1991, *ApJ*, **382**, 433
- Stickel, M., Fried, J. W., & Kuehr, H. 1988, *A&A*, **191**, L16
- Stickel, M., Fried, J. W., & Kuehr, H. 1989, *A&AS*, **80**, 103
- Stickel, M., Fried, J. W., & Kuehr, H. 1993a, *A&AS*, **98**, 393
- Stickel, M., & Kuehr, H. 1993, *A&AS*, **100**, 395
- Stickel, M., & Kuehr, H. 1994, *A&AS*, **105**, 67
- Stickel, M., & Kuehr, H. 1996a, *A&AS*, **115**, 11
- Stickel, M., & Kuehr, H. 1996b, *A&AS*, **115**, 1
- Stickel, M., Kuehr, H., & Fried, J. W. 1993b, *A&AS*, **97**, 483
- Stickel, M., & Kuehr, H. 1993, *A&AS*, **101**, 521
- Stickel, M., Meisenheimer, K., & Kuehr, H. 1994, *A&AS*, **105**, 211
- Stoeckle, J. T., Wurtz, R., Wang, Q., Elston, R., & Jannuzi, B. T. 1992, *ApJL*, **400**, L17
- Stratta, G., Capalbi, M., Giommi, P., et al. 2011, arXiv:1103.0749
- Strauss, M. A., Huchra, J. P., Davis, M., et al. 1992, *ApJS*, **83**, 29
- Strittmatter, P. A., Carswell, R. F., Gilbert, G., & Burbidge, E. M. 1974, *ApJ*, **190**, 509
- Tadhunter, C. N., Morganti, R., di Serego-Alighieri, S., Fosbury, R. A. E., & Danziger, I. J. 1993, *MNRAS*, **263**, 999
- The Fermi-LAT Collaboration, Ajello, M., Angioni, R., et al. 2020, *ApJ*, **892**, 105
- Thompson, D. J., Djorgovski, S., & de Carvalho, R. 1990, *PASP*, **102**, 1235
- Thompson, D. J., Djorgovski, S., Vigotti, M., & Grueff, G. 1992, *ApJS*, **81**, 1
- Tingay, S. J., Preston, R. A., Lister, M. L., et al. 2001, *ApJL*, **549**, L55
- Titov, O., Jauncey, D. L., Johnston, H. M., Hunstead, R. W., & Christensen, L. 2011, *AJ*, **142**, 165
- Torres-Zafra, J., Cellone, S. A., Buzzoni, A., Andruchow, I., & Portilla, J. G. 2018, *MNRAS*, **474**, 3162
- Truebenbach, A. E., & Darling, J. 2017, *ApJS*, **233**, 3
- Tytler, D., & Fan, X.-M. 1992, *ApJS*, **79**, 1
- Ulrich, M.-H., Kinman, T. D., Lynds, C. R., Rieke, G. H., & Ekers, R. D. 1975, *ApJ*, **198**, 261
- Urry, C. M., & Padovani, P. 1995, *PASP*, **107**, 803
- Vandenbroucke, J., Buehler, R., Ajello, M., et al. 2010, *ApJL*, **718**, L166
- Varshalovich, D. A., Levshakov, S. A., Nazarov, E. A., Spiridonova, O. I., & Fomenko, A. F. 1987, *AZh*, **64**, 262
- Vermeulen, R. C., Ogle, P. M., Tran, H. D., et al. 1995, *ApJL*, **452**, L5
- Vermeulen, R. C., Ros, E., Kellermann, K. I., et al. 2003, *A&A*, **401**, 113
- Vermeulen, R. C., Taylor, G. B., Readhead, A. C. S., & Browne, I. W. A. 1996, *AJ*, **111**, 1013
- Veron-Cetty, M. P., & Veron, P. 1996, *ESO Rep.*, **17**, 1
- Véron-Cetty, M. P., & Véron, P. 2000, *A&ARv*, **10**, 81
- Walker, R. C., Hardee, P. E., Davies, F. B., Ly, C., & Junor, W. 2018, *ApJ*, **855**, 128
- Walsh, D., Beckers, J. M., Carswell, R. F., & Weymann, R. J. 1984, *MNRAS*, **211**, 105
- Walsh, D., & Carswell, R. F. 1982, *MNRAS*, **200**, 191
- White, G. L., Jauncey, D. L., Wright, A. E., et al. 1988, *ApJ*, **327**, 561
- White, R. L., Becker, R. H., Gregg, M. D., et al. 2000, *ApJS*, **126**, 133
- Wilkes, B. J. 1986, *MNRAS*, **218**, 331
- Wilkes, B. J., Wright, A. E., Jauncey, D. L., & Peterson, B. A. 1983, *PASAu*, **5**, 2
- Wills, D., & Lynds, R. 1978, *ApJS*, **36**, 317
- Wills, D., & Wills, B. J. 1974, *ApJ*, **190**, 271
- Wills, D., & Wills, B. J. 1976, *ApJS*, **31**, 143
- Wright, A. E., Ables, J. G., & Allen, D. A. 1983, *MNRAS*, **205**, 793
- Wright, A. E., Peterson, B. A., Jauncey, D. L., & Condon, J. J. 1979, *ApJ*, **229**, 73
- Xiong, D., Zhang, X., Bai, J., & Zhang, H. 2015, *MNRAS*, **450**, 3568
- Xu, W., Lawrence, C. R., Readhead, A. C. S., & Pearson, T. J. 1994, *AJ*, **108**, 395
- York, D. G., Adelman, J., Anderson, J. E., Jr., et al. 2000, *AJ*, **120**, 1579
- Zensus, J. A., Ros, E., Kellermann, K. I., et al. 2002, *AJ*, **124**, 662